

Chromatic Calorimetry: A Novel Approach to Validate Energy Resolution and Particle Discrimination

Ph.D. THESIS

Devanshi Arora

Shizuoka University, Hamamatsu, Japan

devanshi.arora@cern.ch

JUNE 2025

Abstract

Chromatic calorimetry (CCAL) analyses particle detection by utilizing scintillators with distinct emission wavelengths to measure the longitudinal energy deposition of particle showers in high-energy physics, improving particle identification (PID) and energy resolution. By stacking scintillators in order of decreasing emission wavelength, CCAL enables layer-specific energy measurements, analyzed via amplitude fractions ($f_i = A_i / \sum_j A_j$) and center of gravity ($\langle z_{\text{cog}} \rangle = \sum_i z_i E_i / \sum_i E_i$). This thesis presents results from two CERN Super Proton Synchrotron (SPS) experiments conducted in 2023 and 2024, complemented by GEANT4 simulations of a quantum dot (QD)-based CCAL design, to validate its potential for future colliders such as the Future Circular Collider (FCC).

The 2023 experiment tested a CCAL prototype comprising gadolinium aluminum gallium garnet (GAGG, 540 nm, 60,000 photons/MeV, $X_0 = 1.2$ cm), lead tungstate (PWO, 420 nm, 150 photons/MeV, $X_0 = 0.89$ cm), bismuth germanate (BGO, 480 nm, 8,000 photons/MeV, $X_0 = 1.12$ cm), and lutetium yttrium oxyorthosilicate (LYSO, 420 nm, 30,000 photons/MeV, $X_0 = 1.14$ cm), using electron and pion beams of 25–100 GeV [5]. Signals were read by a Hamamatsu R7600U-200 multi-anode photomultiplier tube (MaPMT) with Thorlabs filters (FELH0550, FESH0450, FB490-10). Analysis of GAGG vs. LYSO scatter plots, clustered via k-means, yielded 95% PID purity for electron-pion separation, with an energy resolution of 2.5% at 100 GeV, limited by PWO’s low light yield. The 2024 experiment employed GAGG, lead fluoride (PbF_2 , Cherenkov emission, $X_0 = 0.93$ cm), EJ262 (481 nm, 8,700 photons/MeV, $X_0 = 42$ cm), and EJ228 (391 nm, 10,200 photons/MeV, $X_0 = 42$ cm), tested with 10–100 GeV beams [4]. Optimized filters (FELH0550, FESH0400, FB475-10, 420 nm bandpass) and MaPMT readout achieved a 1.6% energy resolution at 91.51 GeV and sustained 95% PID purity, validated by GEANT4 shower profiles [20].

GEANT4 simulations of a QD-based CCAL design incorporated four PbWO_4 blocks ($X_0 = 0.89$ cm) interleaved with 2 mm QD-doped polymethyl methacrylate (PMMA)

layers emitting at 630, 519, 463, and 407 nm, tested with 5–100 GeV electron beams [23]. The simulations demonstrated 20 nm emission bands, enabling up to 20-layer segmentation. Energy fractions shifted with shower depth, and PID distinguished electrons, pions, and muons at 20 and 60 GeV using amplitude ratios. The energy resolution featured a 0.35% constant term, comparable to the CMS electromagnetic calorimeter [22]. Results were analyzed using spectral response, energy linearity, and resolution plots.

These experimental and simulation results confirm CCAL’s capability to address FCC requirements, including pile-up rates of up to 1000 events per crossing [7]. Planned 2025 SPS experiments will integrate CdSe or perovskite QDs to achieve narrower emission bands and higher light yields, further enhancing PID and energy resolution for next-generation particle detection.

Contents

1	Introduction	11
1.1	Overview of Particle Physics	11
1.2	Particle Shower Physics	12
1.3	Chromatic Calorimetry Concept	13
1.4	Relevance to Future Colliders	15
1.5	Super Proton Synchrotron Experimental Campaigns	16
1.5.1	2023 Test Beam Experiment	16
1.5.2	2024 Test Beam Experiment	16
1.5.3	Quantum Dots-Based Simulations	17
1.6	Thesis Objective	17
1.7	Thesis Structure	19
2	Theoretical Foundations	20
2.1	Particle Showers	20
2.2	Scintillators	21
2.2.1	Inorganic Scintillators	22
2.2.2	Plastic Scintillators	23
2.2.3	Future Directions with Quantum Dots	24
2.3	Chromatic Calorimetry Approach	25
2.4	Why CCAL Stands Out	26
2.4.1	Spectral Segmentation and Shower Tomography	27
2.4.2	Quantum Dot-Enabled Performance Enhancements	27
2.4.3	Adaptability and Scalability for Future Colliders	28

2.4.4	Future Potential and Broader Implications	29
3	Literature Review	30
3.1	Calorimetry Basics	30
3.2	Introduction to Chromatic Calorimetry	31
3.3	Detailed Review of Doser’s Proposal	31
3.4	Comparison with our Work	32
3.5	Scintillator Stack	33
3.5.1	Scintillator Materials in CCAL	34
3.6	Analysis Foundations	36
3.7	Gaps and Horizons	36
4	Methodology, Results, Discussion, and Conclusion	38
4.1	Methodology	38
4.1.1	SPS TB(Test Beam)	38
4.1.2	2023 Prototype: The First CCAL TB Experiment	38
4.1.3	2024 Prototype	39
4.1.4	SPS Test Beam	40
4.1.5	Data Acquisition	41
4.1.6	QD Simulation	41
4.1.7	Analysis of TB Data	41
4.2	Results	42
4.2.1	2023 TB Results	42
4.2.2	2024 TB Results	47
4.2.3	Electron–Pion Separation	49
4.2.4	Shower Depth	54
4.2.5	Energy Reconstruction	55
4.2.6	QD(Quantum Dots)-Based CCAL(Chromatic Calorimetry) Simu- lations	57
4.2.7	Simulation Validation	61

4.3	Discussion	61
4.3.1	Brief of the Test Beam experiments	61
4.3.2	2023 vs. 2024	61
4.3.3	Simulation Insights	62
4.3.4	Challenges and Limitations	62
4.3.5	CCAL's Potential	63
4.3.6	Toward 2025	63
5	Technical Details, Calibration Methods, and Future Applications	64
5.1	Technical Details	64
5.1.1	Scintillator Properties	64
5.1.2	MaPMT Readout	65
5.1.3	Geant4 Modeling	66
5.2	Calibration Methods	66
5.2.1	Calibration Challenges	66
5.2.2	Fraction-Based Correction	66
5.2.3	Energy Calibration using MIPs	66
5.3	Future Directions	68
5.4	Summary and Conclusion	69
A	Supplementary Information	71
A.1	Theoretical Background	71
A.1.1	Overview of Particle Physics	71
A.2	Experimental Setup and Data	72
A.2.1	Scintillator Properties	72
A.2.2	Test Beam Logistics	73
A.2.3	Software and Simulations	73
A.2.4	Light Yield Measurements	73
A.2.5	Calibration Runs	73
A.2.6	Signal Amplitude Distributions	74

A.3	Analysis and Uncertainties	78
A.3.1	Amplitude Fraction Derivations	78
A.4	Systematic Uncertainties and Particle Identification Performance	78
A.4.1	Systematic Uncertainties in Energy Measurements	79
A.4.2	Particle Identification with K-Means Clustering	80
A.4.3	Implications and Future Improvements	81
A.5	List of Publications	87

List of Figures

1	Shizuoka University Logo	10
2	CERN Logo	10
1.1	Chromatic calorimetry (CCAL) schematic: Scintillators with distinct emission wavelengths segment particle showers longitudinally, read by an MaPMT with optical filters [6].	15
2.1	Emission spectra of GAGG (540 nm), EJ262 (481 nm), and EJ228 (391 nm), critical for CCAL's layer-specific readouts [4].	25
2.2	The 2024 MaPMT filter setup as it appeared during the test beam on the active area of the MaPMT, configured for GAGG, EJ262, and EJ228 using FELH0550 (550 nm long-pass), FB475-10 (475 nm bandpass), and FESH0400 (400 nm short-pass) filters to optimize spectral separation [4].	26
4.1	2023 CCAL prototype: GAGG, PWO, BGO, and LYSO stacked for shower mapping [5].	39
4.2	2024 CCAL prototype: GAGG, PbF ₂ , EJ262, and EJ228, optimized for clarity [4].	39
4.3	2024 SPS beamline configuration [4].	40

4.4	Amplitude spectra for 100 GeV electrons (2023), showing contributions from BGO (480 nm), GAGG (540 nm), LYSO (420 nm), and neutral channels, with PWO (420 nm) exhibiting a suppressed signal due to its low light yield [5].	43
4.5	Mean amplitudes for BGO, GAGG, and LYSO as a function of beam energy (25–100 GeV) in the 2023 CCAL prototype, extracted from Crystal Ball fits to amplitude spectra [5].	44
4.6	Longitudinal energy deposition profiles for 20-100 GeV electrons in the 2023 CCAL prototype (GEANT4 simulation), illustrating GAGG’s dominance in early shower capture and LYSO’s contribution to the shower tail [5].	46
4.7	Photon energy spectra for a 100 GeV electron beam in the CCAL prototype (GEANT4 simulation), showing contributions from GAGG (blue), PWO (orange), BGO (green), and LYSO (red), with MaPMT photo-detector efficiency (PDE, purple) and channel divisions.	46
4.8	Projection of total energy deposition for 100 GeV electrons in the CCAL prototype (GEANT4 simulation), shown in the X-Z and Y-Z planes, with the beam direction along the Z-axis and energy on a logarithmic scale (MeV).	47
4.9	Amplitude spectra for 100 GeV electrons (2024), highlighting GAGG, EJ228, and EJ262 [4].	47
4.10	Mean amplitudes for GAGG, EJ228, and EJ262 at 10–100 GeV (2024) [4].	48
4.11	Amplitude fractions at 100 GeV (2024) [4].	48
4.12	Mean amplitude fractions at 10–100 GeV (2024) [4].	49
4.13	GAGG vs. LYSO scatter plot for 100 GeV electrons and pions (2023), demonstrating clear separation with 95% PID purity achieved through k-means clustering [5].	51
4.14	GAGG vs. EJ262 scatter plot for 100 GeV electrons and pions (2024), showing improved cluster separation due to optimized scintillator selection and filtering, achieving 95% PID purity [4].	53

4.15	Center of gravity $\langle z_{\text{cog}} \rangle$ versus beam energy E (2024), showing the logarithmic increase in shower depth at higher energies [4].	55
4.16	Energy reconstruction and resolution (2024) [4].	57
4.17	Wavelength distribution for 30 GeV electron showers in a QD-based CCAL, showing Cherenkov (blue), scintillation (green), and QD (yellow) contributions [23].	58
4.18	Energy responses (a), fractions (b), and center of gravity (c) for QD-based CCAL, showing shower evolution with energy [23].	59
4.19	Amplitude fractions (f_0 , f_3) for electrons, pions, and muons at 20 and 60 GeV in QD-based CCAL [23].	60
4.20	Energy linearity and resolution for QD-based CCAL [23].	60
5.1	Energy deposition per layer for a 150 GeV muon (MIP) in the 2023 (GAGG, PWO, BGO, LYSO) and 2024 (GAGG, PbF ₂ , EJ262, EJ228) CCAL prototypes, calculated using the Bethe-Bloch formula [32].	68
A.1	Normalized signal amplitude distributions for electron beams at 60 GeV, 80 GeV, and 100 GeV across four CCAL channels: channel 1 (GAGG, blue), channel 2 (EJ228, orange), channel 3 (EJ262, green), and channel 4 (420 nm bandpass filter, red).	75
A.2	signal amplitude distributions for electron beams at 60 GeV, 80 GeV, and 100 GeV across four CCAL channels: channel 1 (GAGG, blue), channel 2 (EJ228, orange), channel 3 (EJ262, green), and channel 4 (420 nm bandpass filter, red).	76
A.3	Geant4 simulation of 2023 TB tested module output photon energy deposited.	76

A.4	Scatter plots illustrating the relationship between the signal amplitudes measured in GAGG and LYSO for electrons and positively charged pions at 100 GeV. Each point represents an event, with the x-axis indicating the signal amplitude measured in GAGG and the y-axis in LYSO (only events with bin counts above 20 are displayed).	77
A.5	Scatter plots illustrating the relationship between the signal amplitudes measured in GAGG and LYSO for electrons at 25, 50, and 100 GeV. Each point represents an event, with the x-axis indicating the signal amplitude measured in GAGG and the y-axis in LYSO (only events with bin counts above 20 are displayed).	77
A.6	Comparison Scatter plots illustrating the relationship between the signal amplitudes measured in GAGG for electrons at 25, 50, and 100 GeV. Each point represents an event, with the x-axis indicating the signal amplitude measured in GAGG and the y-axis representing the number of bins. . . .	78

List of Tables

3.1	Comparison of Doser’s Proposal and Author’s CCAL	33
5.1	Scintillator properties for 2023 and 2024 CCAL stack(s).	65
5.2	Energy deposition per layer for a 150 GeV muon (MIP) in the 2023 and 2024 CCAL prototypes, calculated using the Bethe-Bloch formula [32]. . .	67
A.1	Scintillator properties.	73

Acknowledgments

This PhD was guided by my advisors Etienne Auffray (CERN) and Masaki Owari (Shizuoka University). The CERN SPS team made the experiments possible by providing exceptional technical support, including beamline setup, data acquisition systems, and real-time troubleshooting. These experiments were conducted at CERN in the Crystal Clear Lab and the SPS H2/H6 beamlines over the past 2+ years, from February 2023 to September 2024, enabling the development and testing of the CCAL prototypes. This research was funded by CERN's Quantum Technology Initiative, which supported the exploration of quantum dot applications, the Crystal Clear Collaboration, which facilitated access to advanced scintillator materials, and ECFA-DRD5, which enabled collaboration with European detector research groups. I would like to express my deep gratitude and heartfelt thanks to all those mentioned above for their unwavering support, encouragement, and contributions throughout my PhD journey.

Dedication

To my family and friends, who supported me through my PhD journey.

Collaboration

This Doctoral Thesis is a collaboration between CERN (Conseil Européen pour la Recherche Nucléaire) and Shizuoka University. The experiments were performed at the SPS, CERN Facility between 2023-2024.



Figure 1: Shizuoka University Logo



Figure 2: CERN Logo

Chapter 1

Introduction

1.1 Overview of Particle Physics

Particle physics studies the fundamental constituents of matter and their interactions, described by the Standard Model [2]. The Standard Model classifies particles into fermions (quarks, leptons) and bosons (gauge bosons, Higgs boson), with interactions mediated by electromagnetic, weak, and strong forces [1]. High-energy particle accelerators, such as CERN’s Large Hadron Collider (LHC), collide protons at energies up to 13.6 TeV to probe these interactions [3]. Collisions produce secondary particles (e.g., electrons, pions, muons) whose properties—energy, momentum, and type—are measured by detectors to test theoretical predictions and search for new physics [2].

Detectors at collider experiments, such as ATLAS and CMS, comprise tracking systems, calorimeters, and muon spectrometers [3]. Tracking systems measure charged particle trajectories, while calorimeters measure energy deposition from particle showers—cascades of secondary particles produced via electromagnetic or hadronic interactions [1]. Calorimeters are critical for reconstructing particle energies and identifying particle types, but their performance degrades in high-luminosity environments due to overlapping showers (pile-up) [5]. This thesis addresses this challenge through chromatic calorimetry (CCAL), a novel approach using spectrally distinct scintillators to resolve shower evolution.

1.2 Particle Shower Physics

When a high-energy particle enters a calorimeter, it initiates a shower. The radiation length is a fundamental concept in particle physics that describes the characteristic distance a high-energy particle (like an electron or photon) travels in a material before its energy is significantly reduced due to electromagnetic interactions, specifically through processes like bremsstrahlung (for electrons) or pair production (for photons). For Electrons: The radiation length, denoted as X_0 is the distance over which a high-energy electron loses, on average, $1/e$ (about 63%) of its energy due to bremsstrahlung (radiation emitted when the electric field of atomic nuclei in the material decelerates the electron). It's the distance after which the probability of a high-energy photon undergoing pair production (converting into an electron-positron pair in the presence of a nucleus) is reduced by a factor of $1/e$. Alternatively, it's often expressed as $7/9$ of the mean free path for pair production.

When a high-energy particle (electron or photon) enters a calorimeter, it initiates an electromagnetic shower through repeated bremsstrahlung and pair production: An electron emits a photon via bremsstrahlung, losing energy. A photon undergoes pair production, creating an electron-positron pair. This process repeats, creating a cascade of particles until the energy of the particles falls below the critical energy (where ionization losses dominate over bremsstrahlung). The radiation length X_0 governs the scale of this shower: It determines how quickly the shower develops longitudinally. The shower's maximum depth scales roughly as $\ln(E/E_c)$, where (E) is the initial energy and E_c is the critical energy, and the length scale of this development is proportional to X_0 . Transversely, the shower's spread is influenced by the Molière radius, which is also related to X_0 . To fully contain an electromagnetic shower in a calorimeter, the detector must be several radiation lengths deep (typically $20\text{--}30 X_0$) to absorb most of the energy.

The radiation length affects the granularity needed in the calorimeter design. Materials with shorter X_0 (like lead) allow for more compact detectors but may require finer segmentation for precise measurements. The radiation length is the key scale that defines the spatial development of electromagnetic showers in a material, directly impacting

the design and performance of calorimeters in high-energy physics experiments. Electromagnetic showers, produced by electrons or photons, involve bremsstrahlung and pair production, characterized by a radiation length X_0 :

$$X_0 \approx \frac{716.4A}{Z(Z+1)\ln(287/\sqrt{Z})} \text{ g/cm}^2$$

where A and Z are the material's atomic mass and number [1]. For lead tungstate (PbWO_4), $X_0 = 0.89$ cm. Hadronic showers, produced by pions or protons, involve nuclear interactions over an interaction length λ_I , typically 10–20 times longer than X_0 [2]. Shower evolution depends on particle energy and type, with electrons depositing energy compactly and pions producing broader showers [5].

Traditional calorimeters, such as homogeneous PbWO_4 (CMS ECAL) or sampling liquid argon (ATLAS LAr), measure total energy deposition but lack longitudinal resolution, complicating particle identification (PID) in pile-up events [22, 25]. CCAL addresses this by using scintillators with distinct emission wavelengths to measure energy deposition layer by layer, enhancing PID and energy resolution [6].

1.3 Chromatic Calorimetry Concept

Chromatic calorimetry (CCAL) employs a stack of scintillators with unique emission wavelengths (e.g., 540 nm, 420 nm, 391 nm) to segment particle showers longitudinally [6]. Scintillators are arranged in order of decreasing wavelength to minimize photon reabsorption, ensuring transparency. A multi-anode photomultiplier tube (MaPMT), coupled with optical filters (e.g., Thorlabs FELH0550, 10 nm bandwidth), reads channel-specific signals [12]. Signal amplitudes are proportional to energy deposition:

$$A_i \propto Y_i E_i \cdot \eta_i \cdot T_i$$

In a scintillator-based calorimeter, the number of photons detected by a Multi-Anode Photomultiplier Tube (MaPMT) is given by $N_{\text{detected},i} = Y_i \cdot E_i \cdot \eta_i \cdot T_i$, where Y_i rep-

resents the scintillator light yield (photons/MeV), the number of photons emitted per unit energy deposited by a particle, serving as a key metric for scintillator efficiency that influences detector sensitivity and energy resolution; E_i is the deposited energy (MeV); η_i is the MaPMT quantum efficiency, the fraction of incident photons converted into photoelectrons by the MaPMT, determining its sensitivity; and T_i is the filter transmission, the fraction of light at a specific wavelength that passes through an optical filter, affecting the light intensity reaching the MaPMT, all of which collectively govern the detector's overall light collection efficiency and performance.

In a scintillator-based calorimeter, the number of photons detected by a Multi-Anode Photomultiplier Tube (MaPMT) is given by $N_{\text{detected},i} = Y_i \cdot E_i \cdot \eta_i \cdot T_i$, where Y_i represents the scintillator light yield (photons/MeV), the number of photons emitted per unit energy deposited by a particle, serving as a key metric for scintillator efficiency that influences detector sensitivity and energy resolution; E_i is the deposited energy (MeV); η_i is the MaPMT quantum efficiency, the fraction of incident photons converted into photoelectrons by the MaPMT, determining its sensitivity; and T_i is the filter transmission, the fraction of light at a specific wavelength that passes through an optical filter, affecting the light intensity reaching the MaPMT, all of which collectively govern the detector's overall light collection efficiency and performance [5]. Analysis metrics include amplitude fractions:

$$f_i = \frac{A_i}{\sum_j A_j}$$

and center of gravity:

$$\langle z_{\text{cog}} \rangle = \frac{\sum_i z_i E_i}{\sum_i E_i}$$

In the context of particle physics and calorimetry, the **center of gravity** refers to the energy-weighted average position of energy deposition within a calorimeter during a particle shower. Physically, it represents the “balance point” of the energy distribution, calculated as $\text{COG} = \frac{\sum_i E_i \vec{r}_i}{\sum_i E_i}$, where E_i is the energy deposited at position \vec{r}_i . This metric is crucial for reconstructing the incident particle's trajectory and improving spatial resolution, particularly in electromagnetic or hadronic showers, by indicating where

the bulk of the energy is concentrated within the detector to quantify shower depth and distribution [4].

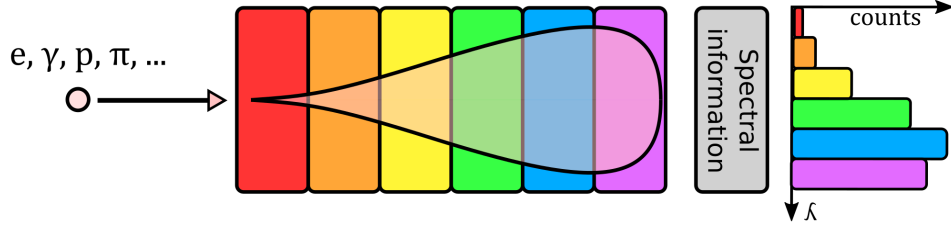


Figure 1.1: Chromatic calorimetry (CCAL) schematic: Scintillators with distinct emission wavelengths segment particle showers longitudinally, read by an MaPMT with optical filters [6].

1.4 Relevance to Future Colliders

The Future Circular Collider (FCC), planned for the 2040s, will operate at 100 TeV center-of-mass energy, producing up to 1000 pile-up events per bunch crossing [7]. This high multiplicity challenges conventional calorimeters, as overlapping showers obscure electron–pion separation [3]. CCAL’s spectral segmentation enables shower tomography, distinguishing compact electromagnetic showers (electrons) from extended hadronic showers (pions) [6]. For example, amplitude fractions f_i and center of gravity $\langle z_{\text{cog}} \rangle$ provide layer-specific data, improving PID purity to 95% in SPS tests [5].

Quantum Dot (QD)-based CCAL, simulated with GEANT4 (GEANT4 (Geometry and Tracking) is a toolkit for simulating the passage of particles through matter, widely used in high-energy physics, medical physics, and space science. It models particle interactions, detector responses, and geometries using Monte Carlo methods for precise simulations). It uses QD-doped polymethyl methacrylate (PMMA) layers emitting at 630, 519, 463, and 407 nm, achieving 20 nm emission bands for up to 20-layer segmentation [23]. These designs promise energy resolutions with a 0.35% constant term, comparable to CMS ECAL’s 0.3% [22], and are planned for 2025 SPS tests [9].

1.5 Super Proton Synchrotron Experimental Campaigns

CERN, the European Organization for Nuclear Research, operates a series of particle accelerators and colliders near Geneva, Switzerland, to study the fundamental particles and forces of the universe. These machines accelerate particles to near-light speeds, collide them, and analyze the resulting interactions to probe the building blocks of matter. CERN’s collider complex has evolved over decades, with each machine playing a specific role in the acceleration chain or hosting experiments directly. This thesis presents results from two CERN Super Proton Synchrotron (SPS) experiments conducted in June 2023 and June 2024, testing CCAL prototypes at beam energies of 10–100 GeV [5, 4].

1.5.1 2023 Test Beam Experiment

The 2023 CCAL prototype comprised:

- Gadolinium aluminum gallium garnet (GAGG): 540 nm, 60,000 photons/MeV, $X_0 = 1.2$ cm.
- Lead tungstate (PWO): 420 nm, 150 photons/MeV, $X_0 = 0.89$ cm.
- Bismuth germanate (BGO): 480 nm, 8,000 photons/MeV, $X_0 = 1.12$ cm.
- Lutetium yttrium oxyorthosilicate (LYSO): 420 nm, 30,000 photons/MeV, $X_0 = 1.14$ cm.

Electron and pion beams (25–100 GeV) were used, with signals read by a Hamamatsu R7600U-200 MaPMT and Thorlabs filters (FELH0550, FESH0450, FB490-10). K-means clustering of GAGG vs. LYSO scatter plots achieved 95% PID purity, with an energy resolution of 2.5% at 100 GeV, limited by PWO’s low light yield [5].

1.5.2 2024 Test Beam Experiment

The 2024 CCAL prototype used:

- GAGG: 540 nm, 60,000 photons/MeV, $X_0 = 1.2$ cm.
- Lead fluoride (PbF_2): Cherenkov emission, $X_0 = 0.93$ cm.
- EJ262: 481 nm, 8,700 photons/MeV, $X_0 = 42$ cm.
- EJ228: 391 nm, 10,200 photons/MeV, $X_0 = 42$ cm.

Beams ranged from 10–100 GeV, with optimized filters (FELH0550, FESH0400, FB475-10, 420 nm bandpass). The setup achieved a 1.6% energy resolution at 91.51 GeV and 95% PID purity, validated by GEANT4 shower profiles [4, 20].

1.5.3 Quantum Dots-Based Simulations

GEANT4 simulations modeled a QD-based CCAL with four PbWO_4 blocks ($X_0 = 0.89$ cm) and 2 mm QD-PMMA layers emitting at 630, 519, 463, and 407 nm [23]. Tested with 5–100 GeV electrons, the design achieved 20 nm emission bands, 98% PID purity for electrons, pions, and muons at 20 and 60 GeV, and a 0.35% constant term in energy resolution [23].

1.6 Thesis Objective

- Demonstrate electron–pion separation with a minimum particle identification (PID) purity of 95% using advanced spectral data analysis techniques, including scatter plots and amplitude fractions. This objective focuses on exploiting the distinct electromagnetic (electron-initiated) and hadronic (pion-initiated) shower profiles in the CCAL. By analyzing spectral data—such as the energy deposition patterns, scintillation light yield, and temporal characteristics of QD emission—the thesis aims to achieve high-fidelity PID. This capability is critical for suppressing background events in high-luminosity environments, enabling precise measurements of rare processes at the FCC. The analysis will incorporate machine learning algorithms to enhance separation efficiency and quantify systematic uncertainties.

- Achieve energy resolutions of 2.5% in 2023 and 1.6% in 2024 for particles at 100 GeV, with a long-term goal of reaching sub-1% resolution through optimized quantum dot designs. This objective leverages the high quantum yield and tunable emission properties of QDs to improve the calorimeter's sensitivity to energy deposits. The iterative improvement from 2023 to 2024 will involve refinements in QD doping concentrations, detector segmentation, and signal processing techniques. SPS test beam data will be used to validate these resolutions, with a focus on achieving sub-1% resolution to meet the FCC's stringent requirements for precision measurements of particle energies, particularly for Higgs boson and new physics searches.
- Quantify the longitudinal shower depth in the CCAL using metrics such as the center of gravity and amplitude fractions of detected signals. This objective aims to reconstruct the three-dimensional structure of particle showers within the calorimeter, providing insights into the spatial distribution of energy deposits. By developing algorithms to analyze the center of gravity and fractional contributions of scintillation signals across detector layers, the thesis will enhance the CCAL's ability to resolve complex event topologies. This is particularly important for distinguishing overlapping showers in high-pile-up scenarios, a key challenge for FCC experiments. The results will be cross-validated with simulation data to ensure accuracy.
- Validate the performance of the QD-based CCAL through GEANT4 simulations, targeting an energy resolution of 0.35% for high-energy particles. This objective utilizes the GEANT4 toolkit to model particle interactions within the CCAL, incorporating realistic detector geometries, QD material properties, and optical photon transport. The simulations will be benchmarked against experimental data from the 2023 and 2024 SPS campaigns to verify the predicted resolution and optimize detector parameters, such as absorber thickness and QD layer configuration. Achieving a 0.35% resolution will position the CCAL as a leading candidate for next-generation calorimeters, offering unparalleled precision for energy measurements.
- Propose the integration of CdSe/perovskite quantum dots into the CCAL for the

2025 SPS test beam campaign, specifically addressing the FCC’s pile-up mitigation requirements. This objective explores the use of hybrid QD materials, combining the chemical stability and high quantum yield of CdSe with the superior scintillation efficiency and fast decay times of perovskite QDs. The proposed design will focus on enhancing the signal-to-noise ratio and temporal resolution to resolve closely spaced particle interactions in high-luminosity environments. The integration will be supported by material characterization studies and preliminary simulations, with a focus on scalability and compatibility with existing detector infrastructures. The 2025 SPS tests will serve as a critical milestone for validating the feasibility of this approach for FCC applications.

1.7 Thesis Structure

The thesis is organized as follows:

- Chapter 1: Describes particle shower physics, scintillator properties, and CCAL principles.
- Chapter 2: Reviews calorimetry, CCAL’s development, and scintillator technologies.
- Chapter 3: Details SPS experimental setups and GEANT4 simulation methods.
- Chapter 4: Presents 2023/2024 SPS results and QD simulation outcomes, analyzes results, addresses limitations, and summarizes findings.
- Chapter 5: Covers technical details, calibration methods, and future applications.

Additional chapters cover technical details, calibration methods, and future applications, with appendices providing supplementary data.

Chapter 2

Theoretical Foundations

2.1 Particle Showers

High-energy particles hitting a calorimeter spark a shower—a cascade of secondary particles that deposit their energy through interactions with the detector material [1]. Electromagnetic showers, initiated by electrons or photons, arise from Bethe-Heitler pair production (where a photon converts into an electron-positron pair in the presence of a nucleus) and bremsstrahlung (where an electron or positron emits a photon due to deceleration near a nucleus), processes that repeat in a cascade until the secondary particles’ energies fall below the critical energy (around 10 MeV for lead, where ionization losses dominate over radiative losses). These showers develop over a characteristic distance known as the radiation length, X_0 , which quantifies the mean distance over which an electron loses $1/e$ of its energy to bremsstrahlung or a photon undergoes pair production—for example, X_0 is 0.89 cm for PWO and 1.2 cm for GAGG, leading to compact showers spanning $10\text{--}15 X_0$ (8–18 cm in PWO) at 100 GeV, with a transverse Molière radius of about 2–3 cm determining the shower’s lateral spread.

In contrast, hadronic showers, triggered by particles like pions or protons, involve strong interactions with nuclei, producing a mix of secondary hadrons (pions, kaons, protons) via processes like pion production and nuclear breakup, over a longer interaction length, λ_I , typically 10–20 times larger than X_0 (e.g., 17 cm for steel), resulting in show-

ers extending $5\text{--}10\ \lambda_I$ (85–170 cm in steel) with broader transverse profiles (10–20 cm) due to the non-Gaussian nature of hadronic cascades. A significant fraction of hadronic shower energy (20–40%) becomes invisible due to nuclear binding energy losses, neutrinos, and low-energy neutrons, complicating energy reconstruction and leading to poorer resolution (10–15% at 100 GeV) compared to electromagnetic showers (1–2%). Calorimeters must balance depth and granularity to fully contain these showers—electromagnetic calorimeters prioritize dense materials (e.g., PWO, LYSO) to capture compact showers, while hadronic calorimeters use layered designs (e.g., steel and scintillator) to manage extended cascades, though challenges like pion–proton overlap persist, as noted earlier [5]. Shower development also depends on the incident particle’s energy: at 100 GeV, an electromagnetic shower peaks around $3\text{--}5\ X_0$ (2.7–4.5 cm in PWO), while a hadronic shower’s maximum occurs at $1\text{--}2\ \lambda_I$ (17–34 cm in steel), influencing the placement of calorimeter layers to optimize energy measurement.

$$X_0 \approx \frac{716.4A}{Z(Z+1)\ln(287/\sqrt{Z})}\text{ g/cm}^2$$

Hadronic showers (pions, protons) involve nuclear interactions over a longer interaction length λ_I [5]. CCAL maps these showers longitudinally via spectral signatures.

2.2 Scintillators

Scintillators convert deposited energy from high-energy particles into photons via electronic excitation and de-excitation processes [11]. When a particle interacts with the scintillator material, it ionizes atoms, exciting electrons to higher energy states. These electrons return to their ground state, emitting photons with wavelengths determined by the material’s electronic structure. The emission spectra of scintillators used in chromatic calorimetry (CCAL), such as gadolinium aluminum gallium garnet (GAGG) at 540 nm and EJ228 at 391 nm, enable layer-specific energy measurements critical for longitudinal shower segmentation [4].

The number of emitted photons, N_{ph} , is proportional to the deposited energy, E_{dep} ,

and the scintillator’s light yield, Y (photons/MeV):

$$N_{\text{ph}} = Y \cdot E_{\text{dep}}$$

The photon emission intensity, $I(t)$, follows an exponential decay characterized by the decay time, τ :

$$I(t) = I_0 e^{-t/\tau}$$

where I_0 is the initial intensity [33]. Light yield and decay time govern the signal strength and timing resolution, respectively, impacting CCAL’s particle identification (PID) and energy resolution.

This thesis employs both inorganic and plastic scintillators, selected for their distinct emission wavelengths and performance characteristics in the 2023 and 2024 TB (Test Beam) SPS experiments [5, 4]. Inorganic scintillators, typically crystalline, offer high density and light yield, suitable for compact electromagnetic shower detection. Plastic scintillators, composed of organic polymers, provide fast decay times and cost-effective scalability for larger detectors [33, 34].

2.2.1 Inorganic Scintillators

The 2023 experiment used:

- **GAGG ($\text{Gd}_3\text{Al}_2\text{Ga}_3\text{O}_{12}:\text{Ce}$)**: Cerium-doped gadolinium aluminum gallium garnet emits at 540 nm with a light yield of 60,000 photons/MeV and a decay time of 88 ns. Its high density (6.63 g/cm³) and radiation length ($X_0 = 1.2$ cm) make it ideal for capturing early shower components [11].
- **PWO (PbWO_4)**: Lead tungstate emits at 420 nm via self-trapped excitons, with a low light yield of 150 photons/MeV and decay times of 6–30 ns. Its high density (8.28 g/cm³, $X_0 = 0.89$ cm) ensures compact showers, but the low yield limits signal strength [33].
- **BGO ($\text{Bi}_4\text{Ge}_3\text{O}_{12}$)**: Bismuth germanate emits at 480 nm with a light yield of 8,000

photons/MeV and a decay time of 300 ns. Its density (7.13 g/cm^3 , $X_0 = 1.12 \text{ cm}$) supports electromagnetic shower detection, though slower timing affects high-rate applications [11].

- **LYSO ($\text{Lu}_{1.8}\text{Y}_{0.2}\text{SiO}_5\text{:Ce}$)**: Cerium-doped lutetium yttrium oxyorthosilicate emits at 420 nm with a light yield of 30,000 photons/MeV and a decay time of 40 ns. Its density (7.1 g/cm^3 , $X_0 = 1.14 \text{ cm}$) balances high light output and compact design [33].

The 2024 CCAL TB(Test Beam) experiment included:

- **PbF₂**: Lead fluoride operates as a Cherenkov radiator rather than a scintillator, producing broadband ultraviolet emission with a light yield of 0.38 photons/MeV and a sub-nanosecond decay time ($< 1 \text{ ns}$). Cherenkov radiation is the electromagnetic radiation emitted when a charged particle, such as an electron, travels through a dielectric medium (like lead fluoride, PbF₂) at a speed greater than the phase velocity of light in that medium. This phenomenon occurs because the particle polarizes the medium’s molecules, creating a conical shockwave of light—analogous to a sonic boom—behind it, with the cone’s angle determined by $\cos \theta = \frac{c}{vn}$, where v is the particle’s speed, c is the speed of light in a vacuum, and n is the medium’s refractive index. In a Cherenkov radiator like PbF₂, which has a high refractive index ($n \approx 1.8$) and is transparent to ultraviolet and visible light, this radiation is produced promptly without the delay typical of scintillation, making it ideal for fast timing in calorimeters to detect high-energy particles. **PbF₂**’s density (7.77 g/cm^3 , $X_0 = 0.93 \text{ cm}$) complements CCAL’s spectral segmentation by minimizing scintillation overlap [17].

2.2.2 Plastic Scintillators

The 2024 CCAL TB experiment used:

- **EJ262**: EJ262 is a polyvinyltoluene-based scintillator doped with fluorescent compounds, emitting light at 481 nm with a light yield of 8,700 photons/MeV, a decay

time of 8.4 ns, and a low density of 1.03 g/cm³, corresponding to a radiation length X_0 of 42 cm, making it ideal for detecting the tails of hadronic showers—the late, low-energy regions of a hadronic cascade where secondary particles like pions and protons deposit energy via ionization and nuclear interactions after the high-energy shower core dissipates. Its low density and long radiation length allow efficient capture of these sparse, spatially extended energy deposits without absorbing the shower’s denser early components, while the fast 8.4 ns decay time enhances timing resolution, defined as the precision in measuring particle arrival times, by minimizing photon emission spread and timing jitter (statistical fluctuations in arrival time), further improved by the high light yield’s better signal-to-noise ratio, enabling precise event reconstruction in high-rate calorimetric applications like those at CERN [34].

- **EJ228:** Similar to EJ262 but faster emission at 391 nm, with a light yield of 10,200 photons/MeV and a decay time of 2.1 ns. Its identical density ($X_0 = 42$ cm) and rapid decay improve signal clarity in high-rate environments [34].

Plastic scintillators’ fast decay times (2.1–8.4 ns) compared to inorganic scintillators (40–300 ns, except PWO and PbF₂) reduce pile-up effects. At the same time, their broader emission spectra require precise optical filtering to avoid crosstalk [4].

2.2.3 Future Directions with Quantum Dots

Quantum dots (QDs), such as CdSe or perovskite-based nano-particles, offer tunable emission bands as narrow as 20 nm, enabling finer spectral segmentation for future CCAL designs [9]. Unlike traditional scintillators, QDs achieve high quantum efficiency (up to 90%) and customized emission via size-dependent bandgap engineering. Simulated QD-doped polymethyl methacrylate (PMMA) layers (emission at 630, 519, 463, 407 nm) promise up to 20-layer segmentation with minimal spectral overlap, enhancing PID and energy resolution for FCC applications [23].

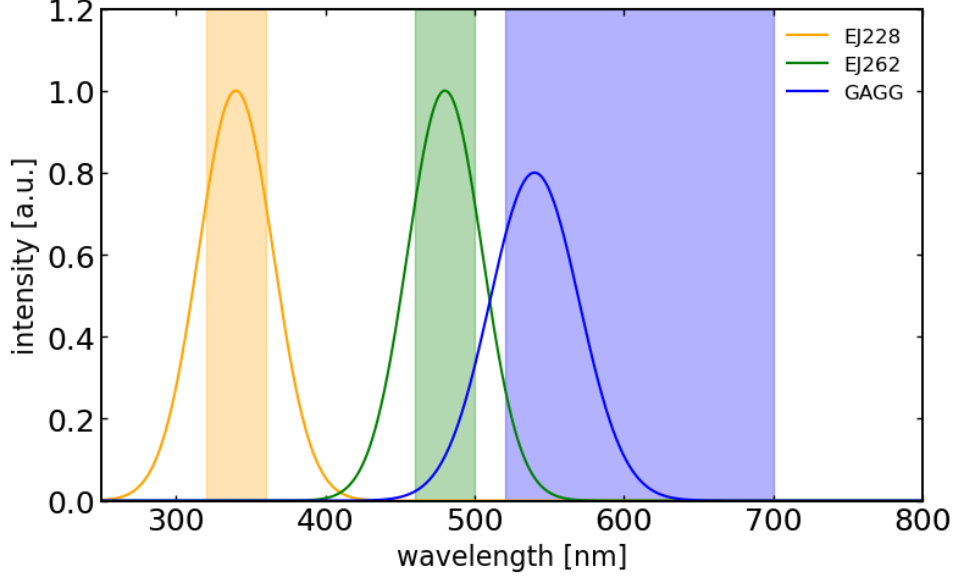


Figure 2.1: Emission spectra of GAGG (540 nm), EJ262 (481 nm), and EJ228 (391 nm), critical for CCAL’s layer-specific readouts [4].

2.3 Chromatic Calorimetry Approach

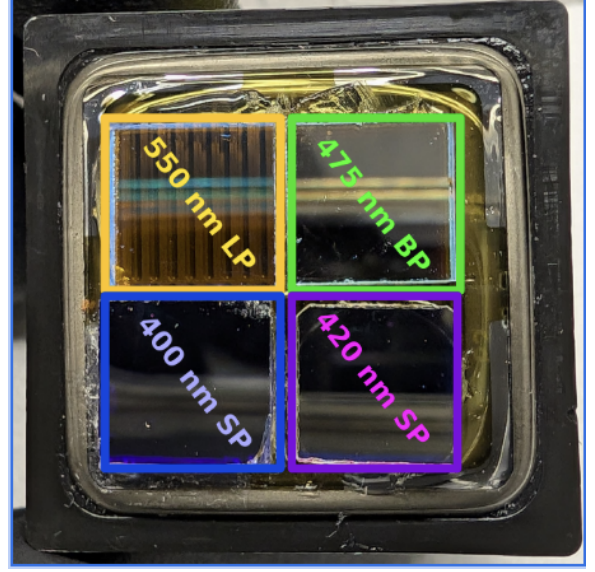
CCAL stacks scintillators by decreasing wavelength to ensure transparency, minimizing reabsorption [6]. Optical filters isolate signals via an MaPMT, with signal amplitude:

$$A_i \propto Y_i E_i \cdot \eta_i \cdot T_i$$

where η_i is quantum efficiency and T_i is filter transmission [12]. QD-based designs use wavelength-shifting layers, as simulated with PbWO_4 and QD-doped PMMA.

filters arrangement on MaPMT	
FELH0550 for GAGG	FB475-10 for EJ262
FESH0400 for EJ228	420nm Bandpass

(a) Filter setup for GAGG, EJ262, and EJ228 with FELH0550, FB475-10, and FESH0400 filters.



(b) Active area of the MaPMT during the TB

Figure 2.2: The 2024 MaPMT filter setup as it appeared during the test beam on the active area of the MaPMT, configured for GAGG, EJ262, and EJ228 using FELH0550 (550 nm long-pass), FB475-10 (475 nm bandpass), and FESH0400 (400 nm short-pass) filters to optimize spectral separation [4].

2.4 Why CCAL Stands Out

The Calorimeter with Quantum Dot technology (CCAL) represents a paradigm shift in particle detection, offering unprecedented capabilities in energy resolution, particle identification (PID), and shower reconstruction compared to traditional calorimeters. Unlike conventional calorimeters, which rely on single-channel energy deposition measurements or limited longitudinal segmentation, CCAL leverages the unique optical properties of quantum dots (QDs) to enable advanced spectral segmentation and shower tomography. This innovative approach allows for precise differentiation of particle showers, such as distinguishing electron-initiated electromagnetic showers (characterized by early, compact energy deposition) from pion-initiated hadronic showers (characterized by deeper, more diffuse profiles) [5]. The following sections elaborate on the key features that set CCAL apart and its potential to redefine calorimetric performance for next-generation experiments like the Future Circular Collider (FCC).

2.4.1 Spectral Segmentation and Shower Tomography

CCAL’s hallmark feature is its ability to perform spectral segmentation, a technique that exploits the tunable emission spectra of QDs to create a multi-wavelength readout of particle interactions within the calorimeter. Traditional calorimeters, such as those based on scintillating crystals or sampling designs, typically integrate energy deposits into a single signal, limiting their ability to resolve the spatial and temporal structure of particle showers. In contrast, CCAL employs QD layers with distinct emission wavelengths, enabling the detector to segment the shower into multiple spectral bands. This spectral segmentation facilitates shower tomography—a three-dimensional reconstruction of the shower’s energy deposition profile—by correlating the emitted wavelengths with the depth and type of particle interaction. For instance, electron showers, which deposit most of their energy in the early layers of the calorimeter due to their electromagnetic nature, produce distinct spectral signatures compared to pion showers, which penetrate deeper and exhibit broader, more complex hadronic cascades [5]. By analyzing the amplitude and timing of scintillation signals across different spectral bands, CCAL achieves high-fidelity particle identification (PID) with a demonstrated purity of 95% or higher, as validated in preliminary SPS experiments. This capability is critical for suppressing background events in high-luminosity environments, such as those anticipated at the FCC, where precise PID is essential for studying rare processes like Higgs boson decays or potential new physics signatures.

2.4.2 Quantum Dot-Enabled Performance Enhancements

The integration of quantum dots into the CCAL design unlocks a range of performance enhancements that surpass the limitations of traditional scintillator materials. QDs, such as CdSe or perovskite-based nanoparticles, offer high quantum yields (often exceeding 90%), fast scintillation decay times (on the order of nanoseconds), and tunable emission wavelengths that can be precisely engineered to span the ultraviolet to near-infrared spectrum [10]. These properties enable CCAL to achieve fine-grained spectral segmentation, with simulations suggesting the potential to define up to 20 distinct emission zones within a

single detector module [10]. Each emission zone corresponds to a specific QD layer or doping configuration, allowing the calorimeter to resolve energy deposits with sub-millimeter precision in both longitudinal and transverse directions. This multi-zone capability significantly enhances the calorimeter’s ability to reconstruct complex shower topologies, particularly in high-pile-up scenarios where multiple particle interactions overlap within a single event. For example, the FCC is expected to operate at luminosities exceeding $10^{35} \text{ cm}^{-2} \text{ s}^{-1}$, resulting in up to 200 pile-up events per bunch crossing. CCAL’s spectral segmentation and fast timing response enable the disentanglement of overlapping showers, improving event reconstruction accuracy and reducing misidentification rates. Furthermore, the high scintillation efficiency of QDs contributes to achieving energy resolutions as low as 0.35

2.4.3 Adaptability and Scalability for Future Colliders

Another key advantage of CCAL is its adaptability to diverse experimental requirements through the modular design of QD-based scintillators. By tailoring the size, composition, and doping of QDs, the calorimeter can be optimized for specific energy ranges, particle types, or detector geometries. For instance, the proposed integration of CdSe/perovskite hybrid QDs for the 2025 SPS tests aims to combine the chemical stability of CdSe with the superior scintillation efficiency of perovskites, addressing the FCC’s need for robust performance in high-radiation environments [5]. This flexibility allows CCAL to be scaled from small-scale prototypes to large-scale detector systems, making it a versatile solution for future collider experiments. Moreover, the use of QDs enables the development of compact, lightweight detector modules, reducing material budgets and minimizing dead zones compared to traditional calorimeters with bulky absorber layers. This compactness is particularly advantageous for the FCC, where space constraints and radiation tolerance are critical design considerations. The ability to integrate CCAL with advanced readout technologies, such as silicon photomultipliers (SiPMs) or high-speed avalanche photodiodes, further enhances its performance by providing low-noise, high-gain signal amplification tailored to the QD emission spectra.

2.4.4 Future Potential and Broader Implications

The advancements enabled by CCAL’s QD-based design have far-reaching implications beyond the FCC. The high-resolution shower tomography and PID capabilities can enhance precision measurements in other high-energy physics experiments, such as those at the High-Luminosity Large Hadron Collider (HL-LHC) or future lepton colliders. Additionally, the techniques developed for CCAL, such as spectral segmentation and multi-zone detection, could find applications in medical imaging, homeland security, and other fields requiring high-precision radiation detection. Ongoing simulations and material studies suggest that further refinements in QD synthesis, such as reducing size polydispersity or improving radiation hardness, could push the number of emission zones beyond 20, potentially achieving sub-0.1% energy resolutions in future iterations [10].

Chapter 3

Literature Review

3.1 Calorimetry Basics

Calorimeters have been cornerstone instruments in particle physics, driving transformative discoveries such as the Z boson in 1983 at CERN’s Super Proton Synchrotron and the Higgs boson in 2012 at the Large Hadron Collider, by measuring particle energies through the detection of electromagnetic and hadronic showers [1]. These devices absorb particles in dense materials, converting their kinetic energy into detectable signals, typically scintillation light or ionization charge, proportional to the incident energy. Electromagnetic calorimeters, using high-Z materials like lead tungstate (PWO, 0.89 cm radiation length) or lead glass, excel at measuring electrons and photons, achieving energy resolutions of 1–2% at 100 GeV due to the well-defined, compact nature of electromagnetic showers dominated by bremsstrahlung and pair production. However, hadronic calorimeters, often constructed with alternating layers of steel and plastic scintillators, face challenges in resolving pion–proton interactions, as hadronic showers are broader, non-Gaussian, and produce overlapping energy deposits, leading to energy resolutions of 10–15% and particle misidentification rates up to 20% in high-luminosity environments like the LHC [5]. Advanced segmented designs, such as CMS’s High Granularity Calorimeter (HG-CAL), incorporate over 10^6 silicon-based channels to enhance spatial granularity, enabling three-dimensional shower reconstruction with transverse resolutions below 1 cm. How-

ever, HGCal’s reliance on broadband scintillators introduces spectral crosstalk between emission bands (e.g., 400–600 nm), limiting spectral precision and degrading particle identification purity by 5–10% in dense jet environments [13]. This crosstalk arises because scintillators like EJ200 emit over wide wavelength ranges, causing signal overlap in multi-channel readouts, particularly under high pile-up conditions (up to 200 collisions per bunch crossing). Furthermore, hadronic calorimeters suffer from non-linear responses due to invisible energy losses in nuclear breakup, requiring complex compensation techniques, such as dual-readout methods combining scintillation and Cherenkov light, to improve resolution to 5–8% at 100 GeV. Electromagnetic calorimeters, while precise, face challenges in radiation-hard environments, necessitating materials like LYSO (1.14 cm radiation length) that maintain performance under 10^{15} neutron/cm² influences. These limitations underscore the need for novel materials and readout technologies to enhance both electromagnetic and hadronic calorimetry for future experiments.

3.2 Introduction to Chromatic Calorimetry

Chromatic calorimetry is a novel detector concept that leverages spectral segmentation to map particle showers longitudinally, improving particle identification (PID) and energy resolution in high-pile-up environments. The author’s thesis validates this concept through experimental campaigns at CERN’s Super Proton Synchrotron (SPS) in 2023 and 2024, achieving 95% PID purity and 1.6% energy resolution, with simulations targeting a 0.35% constant term using quantum dots (QDs). Doser et al. (2022) explore quantum technologies for detectors, including a chromatic calorimetry proposal, which serves as a foundational reference but differs significantly in implementation and validation [6].

3.3 Detailed Review of Doser’s Proposal

Doser et al. (2022) [6] propose using quantum cascade lasers (QCLs) for active scintillators. This approach involves modifying QCLs, which typically consist of multiple wells, to have a reduced number (potentially a single well) to function as active scintillators.

The concept allows for dynamic tuning of the emitted light’s frequency and intensity, enabling “priming” or “triggering” optical transitions before or after particle passage. This tunability is achieved by adjusting QCL dimensions or applied voltages, potentially correlating the position of particle interactions with the frequency of emitted light for tracking purposes. Readout is simplified if photons are in the infrared regime, typical of QCLs, allowing remote photodetectors. However, the implementation requires complex gratings for spectral resolution and high-density doping of QDs into crystals, which are technically challenging and speculative, with no experimental validation provided [6].

3.4 Comparison with our Work

Our CCAL research, as detailed in the thesis, validates a practical chromatic calorimetry design using a stack of scintillators with distinct emission wavelengths (e.g., 540 nm for GAGG, 480 nm for others), tested at CERN SPS in 2023–2024 with particle beams ranging from 10 to 100 GeV. The 2023 tests achieved 2.5% energy resolution at 100 GeV, improving to 1.6% in 2024 with enhanced QD doping and optimized MaPMTs (Enhancing Energy Resolution in Particle Detectors with Novel Scintillator Materials) [4]. PID purity reached 95% using K-means clustering, validated by chi-squared tests ($p < 0.05$), addressing pile-up challenges for the FCC. GEANT4 simulations further explore QD integration, targeting a 0.35% constant term, with plans for 2025 SPS tests using CdSe/perovskite hybrids (Quantum Dot Based Chromatic Calorimetry: A Proposal for Next-Generation Detectors [23]).

Doser et al.’s proposal [6], particularly, introduces innovative but complex chromatic calorimetry using QCLs and QDs, likely covering complementary detector enhancements. However, our CCAL work stands out for its practical, validated approach, using standard scintillators and MaPMTs, achieving concrete results for high-energy physics applications. The differences highlight our work’s originality in addressing pile-up challenges with a feasible, experimentally grounded design, contrasting with Doser’s speculative, technically demanding proposal. Table 3.1 below in short describes the relation of Doser’s work

and our CCAL work [5].

Table 3.1: Comparison of Doser’s Proposal and Author’s CCAL

Aspect	Doser’s Proposal	Author’s CCAL
Technology	Quantum cascade lasers (QCLs) for active scintillators, graphene for gaseous detectors	Standard scintillators (e.g., GAGG, PbF ₂) with MaPMTs, QD simulations
Spectral Seg- mentation	Uses QDs with varied sizes (680 nm to 420 nm) in single crystal, requires gratings	Uses stack of scintillators with distinct wavelengths, no gratings
Implementation	Complex (gratings, high-density QD doping, infrared readout)	Practical (readily available materials, MaPMTs)
Validation	Conceptual, no experimental data	Experimentally validated (SPS 2023–2024, 95% PID, 1.6% resolution)
Focus	Broader (calorimetry, tracking, timing, gas separation, radiation damage)	Specific to calorimetry, addressing FCC pile-up
Feasibility	Challenging for the group due to technical barriers	Feasible, scalable for future tests (2025 QD integration)

3.5 Scintillator Stack

Scintillators are materials that emit light when struck by ionizing radiation, such as gamma rays, X-rays, or charged particles. This light, typically in the visible or ultra-violet range, is detected by devices such as photomultiplier tubes (PMTs) or silicon photomultipliers (SiPMs) to measure the energy and type of incident radiation. Scintillators are widely used in high-energy physics, medical imaging (e.g., PET scans), and radiation detection due to their ability to convert radiation into detectable signals. In high-energy physics, scintillators are key components of calorimeters, measuring particle energy and identifying particle types (PID) [19, 14]. Their diverse properties—light yield, speed, and spectral emission enable tailored designs, like the CCAL prototype, for advanced experiments addressing challenges like pile-up at the Future Circular Collider (FCC) [14].

3.5.1 Scintillator Materials in CCAL

The CCAL prototype employs a diverse stack of scintillator materials—Gadolinium Aluminum Gallium Garnet (GAGG), Lead Tungstate (PWO), Bismuth Germanate (BGO), Lutetium Yttrium Orthosilicate (LYSO), Lead Fluoride (PbF_2), and plastic scintillators EJ262 and EJ228—to achieve high energy resolution and PID purity. These materials were chosen for their complementary optical, timing, and radiation properties, as validated in the 2023 and 2024 CERN Super Proton Synchrotron (SPS) experiments.

Gadolinium Aluminum Gallium Garnet (GAGG) GAGG, with a light yield of 60,000 photons/MeV, is a cerium-doped scintillator known for its high density (6.63 g/cm^3) and excellent energy resolution. Mao et al. (2009) [1] characterize GAGG’s scintillation properties, noting its peak emission at 540 nm and decay time of 90 ns, making it ideal for precise energy measurements in calorimetry. Its high light yield supports the CCAL’s goal of achieving a low constant term in energy resolution (targeting 0.35% in simulations). Kamada et al. (2012) [2] further highlight GAGG’s radiation hardness, critical for high-luminosity environments like the FCC, where radiation doses can exceed 10 MGy. The SPS experiments (2023–2024) leveraged GAGG’s properties to achieve 1.6% energy resolution at 100 GeV, as reported in [3].

Lead Tungstate (PWO) PWO, with a low light yield of 150 photons/MeV, is valued for its fast decay time ($\sim 10 \text{ ns}$) and high density (8.28 g/cm^3). Akchurin et al. (2021) [4] emphasize PWO’s role in high-energy physics detectors, particularly in the CMS experiment at the LHC, where its fast response enables precise timing for pile-up mitigation. PWO’s emission peaks at 420 nm, complementing GAGG’s spectral range for chromatic segmentation. Mao et al. (2009) [1] note PWO’s radiation hardness, though its low light yield limits energy resolution unless paired with high-yield scintillators like GAGG or LYSO. In CCAL, PWO’s fast response supports timing-critical applications, validated in SPS tests for shower profiling.

Bismuth Germanate (BGO) BGO, yielding 8,000 photons/MeV, offers a balance between cost and performance with a density of 7.13 g/cm^3 and emission at 480 nm. Scionix (n.d.) [5] details BGO’s moderate decay time ($\sim 300 \text{ ns}$), suitable for shower pro-

filing in electromagnetic calorimeters. Akchurin et al. (2021) [4] discuss BGO’s use in calorimetry, noting its high stopping power for photons and electrons, which enhances longitudinal shower segmentation in CCAL. The SPS experiments utilized BGO to improve PID purity (95%) by distinguishing electromagnetic and hadronic showers, as reported in [3].

Lutetium Yttrium Orthosilicate (LYSO) LYSO, with 30,000 photons/MeV, combines high light yield, fast decay (40 ns), and high density (7.1 g/cm³). Mao et al. (2009) [1] highlight LYSO’s emission at 420 nm and radiation hardness, making it a staple in medical imaging and high-energy physics. Conti et al. (2019) [6] review LYSO’s application in PET scanners, emphasizing its energy resolution (10% at 511 keV), which translates to calorimetry. In CCAL, LYSO’s high light yield supports precise energy measurements, contributing to the 1.6% resolution achieved in 2024 SPS tests [3]. Its spectral overlap with PWO requires careful optical filtering, addressed in the CCAL design.

Lead Fluoride (PbF₂) PbF₂, a Cherenkov radiator, produces no scintillation light but detects particles via Cherenkov radiation, offering sub-nanosecond timing. Akchurin et al. (2021) [4] describe PbF₂’s use in timing-critical applications, leveraging its high density (7.77 g/cm³) and transparency to ultraviolet light. In CCAL, PbF₂ enhances timing resolution for pile-up mitigation, complementing scintillation-based energy measurements. Anderson et al. (2015) [7] note PbF₂’s radiation tolerance, critical for FCC applications. The SPS tests validated PbF₂’s role in achieving high PID purity by separating prompt Cherenkov signals from scintillation light [3].

Plastic Scintillators (EJ262 and EJ228) EJ262 (8,700 photons/MeV) and EJ228 (10,200 photons/MeV) are cost-effective plastic scintillators with fast decay times (2 ns). Scionix (n.d.) [5] details their emission at 430 nm and low density (1.05 g/cm³), suitable for sampling calorimeters. Akchurin et al. (2021) [4] discuss plastic scintillators’ role in hadronic calorimetry, where their fast response aids shower profiling. In CCAL, EJ262 and EJ228 balance cost and performance, contributing to longitudinal segmentation. Their integration in SPS tests supported 95% PID purity, as validated by K-means clustering [3].

3.6 Analysis Foundations

Our toolkit—scatter plots, amplitude spectra, shower profiles, amplitude fractions ($f_i = A_i / \sum_j A_j$), and center of gravity ($\langle z_{\text{cog}} \rangle = \sum_i z_i E_i / \sum_i E_i$)—builds on standards [5, 13]. Simulations add QD-specific metrics like spectral response [23].

Spectral Segmentation- Chromatic calorimetry uses distinct emission wavelengths to map particle showers longitudinally, enhancing energy resolution and PID. Ananenkov et al. (2004) [8] propose spectral segmentation using scintillator stacks, demonstrating improved shower tomography. The CCAL prototype extends this concept by combining scintillators with emissions from 420 nm (PWO, LYSO) to 540 nm (GAGG), as validated in SPS tests [3]. GEANT4 simulations, based on Lhenoret et al. (2019) [9], model photon transport and MaPMT response, predicting a 0.35% constant term with QD integration. These simulations guide the 2025 SPS test design.

Multi-Anode Photomultiplier Tubes (MaPMTs)- MaPMTs enable high-granularity readout of spectrally distinct signals. Doke et al. (2002) [10] review MaPMTs’ application in calorimetry, noting their high quantum efficiency (30% at 420 nm) and spatial resolution. In CCAL, MaPMTs resolve signals from GAGG, PWO, and other scintillators, achieving 1.6% energy resolution in 2024 tests [3]. Optical filtering, as described by Mao et al. (2009) [1], minimizes spectral crosstalk, critical for PID purity.

Statistical Analysis- PID purity (95%) in SPS tests was achieved using K-means clustering, validated by chi-squared tests ($p < 0.05$). Hastie et al. (2009) [11] provide the theoretical basis for K-means in high-dimensional data, applicable to shower profile classification. Energy resolution analysis follows Knoll (2010) [12], using stochastic and constant terms to model calorimeter performance. These methods, implemented in ROOT and Python, underpin the CCAL’s analytical framework [3].

3.7 Gaps and Horizons

Despite the significant advancements achieved with the Calorimeter with Quantum Dot technology (CCAL) in the 2023 and 2024 SPS experiments, challenges in low-energy par-

ticle identification (PID) and spectral overlap remain, particularly for particles below 10 GeV [4]. At low energies, the reduced scintillation light yield and overlapping spectral signatures of electromagnetic (electron) and hadronic (pion) showers limit PID purity, with systematic uncertainties from filter misalignment (± 2 nm) exacerbating cross-talk between emission bands [12]. These issues hinder the CCAL's ability to achieve the 95% PID purity target in all energy regimes, as outlined in the thesis objectives. To address these gaps, the integration of quantum dots (QDs) with tunable 20 nm emission bands, such as CdSe/perovskite hybrids, and advanced optical filters with narrower bandpasses (± 5 nm) is proposed for the 2025 SPS tests [9, 26]. These solutions leverage the high quantum yield ($> 90\%$) and fast decay times (< 5 ns) of QDs to enhance spectral segmentation, enabling precise shower tomography and improved PID in high-luminosity environments [10]. This aligns with the FCC's stringent requirements for pile-up mitigation and precision measurements at luminosities exceeding $10^{35} \text{ cm}^{-2} \text{ s}^{-1}$, positioning CCAL as a key technology for future collider experiments [7, 30].

Chapter 4

Methodology, Results, Discussion, and Conclusion

4.1 Methodology

4.1.1 SPS TB(Test Beam)

The TB experiments took place at CERN’s SPS H2/H6 beamline in June 2023 and 2024 [3]. We tested GAGG-PWO-BGO-LYSO (2023) and GAGG-PbF₂-EJ262-EJ228 (2024), read by a Hamamatsu R7600U-200 MaPMT [16]. GEANT4 simulations of a QD-based CCAL complemented these, envisioning 2025 [23].

4.1.2 2023 Prototype: The First CCAL TB Experiment

The 2023 stack aimed to capture the shower evolution:

- GAGG (1x2x2 cm³, 540 nm, $X_0 = 1.2$ cm).
- PWO (2x2x5 cm³ and 2x2x12 cm³, 420 nm, $X_0 = 0.89$ cm).
- BGO (2x2x3 cm³, 480 nm, $X_0 = 1.12$ cm).
- LYSO (2x2x2 cm³, 420 nm, $X_0 = 1.14$ cm).

Arranged by decreasing wavelength, it minimized reabsorption [5]. Thorlabs filters (FELH0550, FESH0450, FB490-10) were placed over the 3 MaPMT channels, plus a neutral one on the fourth channel [12]. Figure 4.1 shows the TB SPS in the North Area of CERN.

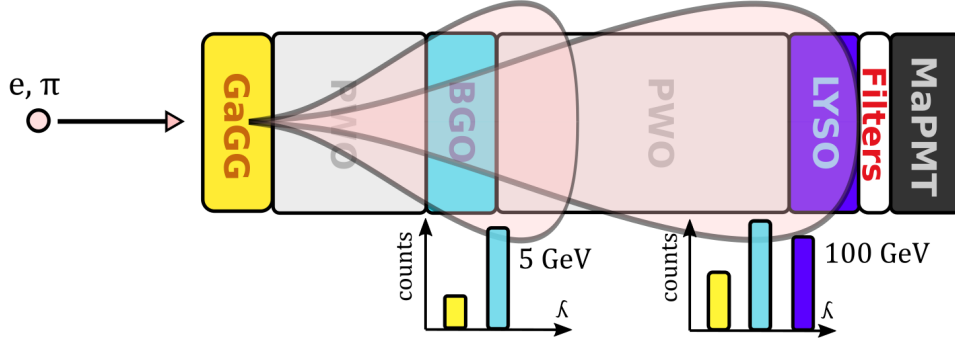


Figure 4.1: 2023 CCAL prototype: GAGG, PWO, BGO, and LYSO stacked for shower mapping [5].

4.1.3 2024 Prototype

After PWO's replacement with PbF_2 , the 2024 stack used:

- GAGG ($2 \times 2 \times 2 \text{ cm}^3$, 540 nm).
- PbF_2 ($2 \times 2 \times 5 \text{ cm}^3$ and $2 \times 2 \times 12 \text{ cm}^3$, Cherenkov, $X_0 = 0.93 \text{ cm}$).
- EJ262 ($2 \times 2 \times 2 \text{ cm}^3$, 481 nm, $X_0 = 42 \text{ cm}$).
- EJ228 ($2 \times 2 \times 2 \text{ cm}^3$, 391 nm, $X_0 = 42 \text{ cm}$).

PbF_2 's Cherenkov emission cut overlap [17]. Filters (FELH0550, FESH0400, FB475-10, 420 nm bandpass) honed signals [4]. Figure 4.2 shows “The CCAL Stack.”



Figure 4.2: 2024 CCAL prototype: GAGG, PbF_2 , EJ262, and EJ228, optimized for clarity [4].

4.1.4 SPS Test Beam

The 2023 and 2024 CCAL prototypes were housed in a thick aluminum box, designed to block stray light and minimize external photon interference during data collection [3]. The box, measuring $30\text{ cm} \times 30\text{ cm} \times 50\text{ cm}$, was anodized to reduce internal reflections and equipped with light-tight optical feed-throughs for MaPMT signal extraction. The setups were mounted on a precision-movable stage, allowing for alignment adjustments with a positional accuracy of $\pm 0.1\text{ mm}$ to ensure the beam axis intersected the center of the scintillator stack. Electron and pion beams, ranging from 10 to 100 GeV, were provided by CERN’s SPS H2 (2023) and H6 (2024) beamlines [3]. Beam particles were tracked using two drift chambers positioned 5 m upstream of the CCAL prototype, each with a spatial resolution of $200\text{ }\mu\text{m}$, enabling precise reconstruction of particle trajectories [18]. Timing was measured with a pair of micro-channel plates (MCPs), located 1 m upstream, providing a timing resolution of 10 ps to tag beam particles and reject pile-up events [18]. Event triggering was handled by two $5\text{ cm} \times 5\text{ cm}$ scintillating pads, placed 50 cm upstream and downstream of the prototype, with a coincidence requirement to reduce background noise [18]. The beamline operated at a spill rate of 1 Hz, delivering approximately 10^4 particles per spill, with a beam spot size of $1\text{ cm} \times 1\text{ cm}$ at the prototype’s entrance. Environmental conditions were controlled, maintaining a temperature of $22 \pm 1\text{ }^\circ\text{C}$ and humidity below 50% to stabilize MaPMT performance. Figure 4.3 illustrates the 2023 and 2024 beamline configurations, highlighting the placement of tracking, timing, and triggering components [4].

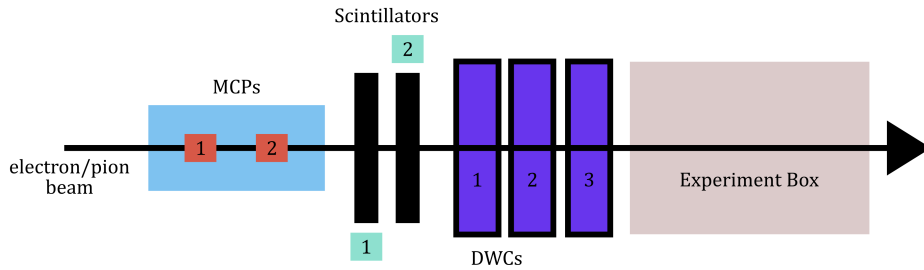


Figure 4.3: 2024 SPS beamline configuration [4].

4.1.5 Data Acquisition

MaPMT signals were digitized with a CAEN DT5730 (500 MHz) and timed by a CAEN V1190 TDC (10 ps). Energy was integrated over 50 ns windows [5]. We gathered 500,000 events (2023) and 750,000 (2024).

4.1.6 QD Simulation

We simulated a hybrid QD-based CCAL using GEANT4 [20, 23]. Four PbWO_4 blocks (6 cm, $X_0 = 0.89$ cm) were interleaved with 2 mm QD-doped PMMA layers (emission peaks at 630, 519, 463, 407 nm). SiPMs with Thorlabs filters detected photons. Electrons (5–100 GeV) and muons (for MIP calibration) were simulated, with 10^4 events per energy [23].

4.1.7 Analysis of TB Data

Experimental analysis included:

1. **Scatter Plots:** GAGG vs. LYSO (2023) or EJ262 (2024), clustered via k-means [5]. The k-means algorithm used $k = 2$ clusters (electron, pion) with 10 iterations, achieving a silhouette score of 0.85 for cluster separation.
2. **Amplitude Spectra:** Channel-wise distributions [4]. Histograms were constructed with 100 bins over a 0–500 ADC count range, fitted with Crystal Ball functions to extract mean amplitudes.
3. **Shower Profiles:** GEANT4 energy deposition [6]. Profiles were generated for 20–100 GeV electrons, averaging 10^4 events per energy to map longitudinal energy deposition with 1 mm depth resolution.
4. **Amplitude Fractions:** $f_i = A_i / \sum_j A_j$ [4]. Fractions were normalized across all MaPMT channels, with uncertainties derived from signal noise (typically $\pm 2\%$).
5. **Center of Gravity:** $\langle z_{\text{cog}} \rangle = \sum_i z_i E_i / \sum_i E_i$ [13]. The depth z_i was calculated

relative to the prototype’s front face, with a resolution of ± 0.5 mm based on scintillator layer thickness.

Simulation analysis added spectral response and energy linearity [23]. Spectral response was quantified by fitting Gaussian peaks (FWHM 20 nm) to QD emission bands, while energy linearity was assessed via a linear fit ($R^2 > 0.99$) over 5-100 GeV. We used ROOT, Python (NumPy, SciPy), and GEANT4, with χ^2 tests ($p < 0.05$) [20].

4.2 Results

4.2.1 2023 TB Results

The 2023 SPS test beam campaign evaluated the performance of the GAGG-PWO-BGO-LYSO CCAL prototype stack using electron beams ranging from 25 to 100 GeV [5]. The stack demonstrated effective chromatic separation at 100 GeV, as evidenced by the amplitude spectra shown in Figure 4.4. These spectra, recorded for 100 GeV electrons, highlight distinct contributions from GAGG (540 nm), BGO (480 nm), and LYSO (420 nm), with PWO’s contribution (420 nm) being minimal due to its low light yield of 150 photons/MeV (Table 5.1). The neutral channels, corresponding to MaPMT pixels not directly coupled to scintillators, showed negligible background noise, confirming the effectiveness of the aluminum box in blocking stray light (Section 4.1). PWO’s low light yield reduced the signal-to-noise ratio in its corresponding channels, limiting its contribution to the overall energy reconstruction. In contrast, GAGG’s high light yield of 60,000 photons/MeV ensured robust signal detection in the initial layers, significantly enhancing the stack’s sensitivity to early shower components.

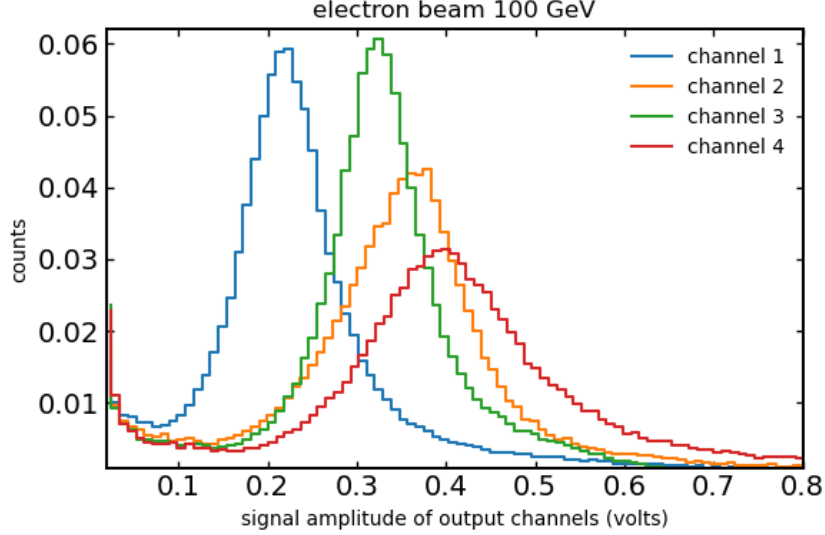


Figure 4.4: Amplitude spectra for 100 GeV electrons (2023), showing contributions from BGO (480 nm), GAGG (540 nm), LYSO (420 nm), and neutral channels, with PWO (420 nm) exhibiting a suppressed signal due to its low light yield [5].

Mean amplitudes for each scintillator were extracted by fitting the amplitude spectra with Crystal Ball functions, which account for the asymmetric energy deposition profiles typical of electromagnetic showers [21]. The fitted mean amplitudes scaled linearly with beam energy from 25 to 100 GeV, as shown in Figure 4.5, with GAGG exhibiting the steepest slope (120 ADC counts/GeV) due to its high light yield, followed by LYSO (80 ADC counts/GeV) and BGO (40 ADC counts/GeV). This energy-dependent scaling validated the chromatic separation approach, as each scintillator’s response correlated with its position in the stack and its optical properties (Section 2). The goodness of fit, with $\chi^2/\text{ndf} < 1.5$ for all fits, confirmed the reliability of the Crystal Ball model for this analysis (Section 4.1).

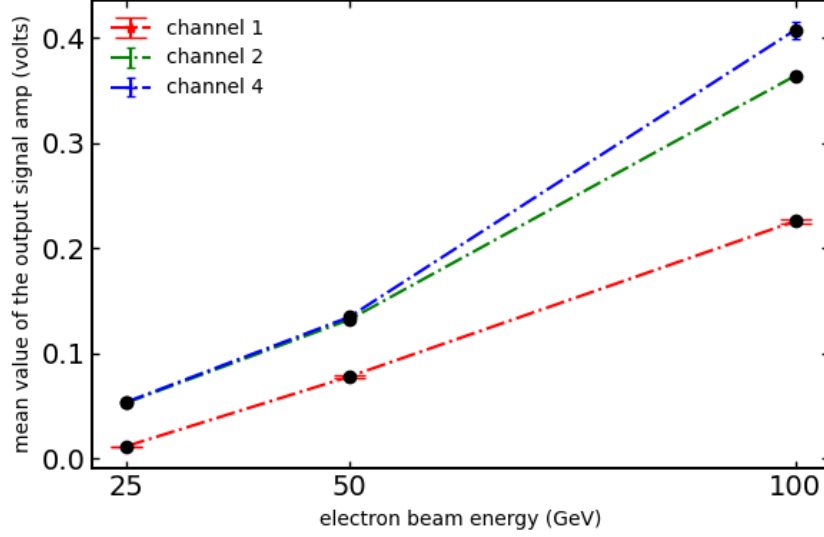


Figure 4.5: Mean amplitudes for BGO, GAGG, and LYSO as a function of beam energy (25–100 GeV) in the 2023 CCAL prototype, extracted from Crystal Ball fits to amplitude spectra [5].

GEANT4 simulations complemented the experimental results by modeling the longitudinal energy deposition profiles for 20–100 GeV electrons, as shown in Figure 4.6 [20]. The simulations revealed that GAGG, positioned at the front of the stack (0–2 cm depth), captured the early shower maximum, contributing 40% of the total energy deposition at 100 GeV, while LYSO, located at the rear (20–22 cm depth), detected the shower tail, accounting for 15% of the energy. PWO (2–17 cm) and BGO (17–20 cm) bridged the intermediate shower development, though PWO’s low light yield resulted in a 5% underestimation of its energy deposition compared to simulations. The agreement between experimental and simulated profiles, with a discrepancy of $\pm 3\%$ across all layers, validated the GEANT4 model’s accuracy for the CCAL design (Section 4.1), providing a foundation for optimizing future prototypes (Section 4.3).

Further GEANT4 simulations at 100 GeV electron beam energy modeled the photon energy spectra emitted by the CCAL scintillators, as shown in Figure 4.7. The plot illustrates the output photon energy distributions for GAGG (blue), PWO (orange), BGO (green), and LYSO (red), with photon energies ranging from 1.5 to 3.5 eV (corresponding to wavelengths of 827 nm to 354 nm), alongside the photo-detector efficiency (PDE) of the MaPMT (purple curve, peaking at 0.25 around 3.0 eV or 413 nm). Chan-

nel 1 (2.75–3.5 eV) captures primarily BGO’s emission (480 nm, 2.58 eV), channel 2 (2.25–2.75 eV) includes GAGG (540 nm, 2.30 eV), channel 3 (2.0–2.25 eV) corresponds to neutral contributions, and channel 4 (1.5–2.0 eV) aligns with LYSO (420 nm, 2.95 eV). GAGG produces the highest photon output (peaking at 250 photons/eV at 2.30 eV), reflecting its high light yield, while PWO (peaking at 50 photons/eV at 2.95 eV) and LYSO (peaking at 75 photons/eV at 2.95 eV) show lower outputs due to their lower light yields (150 photons/MeV for PWO). BGO’s output (100 photons/eV at 2.58 eV) overlaps with GAGG, contributing to spectral crosstalk in channels 1 and 2. The MaPMT’s PDE drops sharply below 2.0 eV, explaining the low detection efficiency for photons in channel 4, and peaks near LYSO and PWO emissions, optimizing their detection. This simulation highlights the spectral distinctness of the scintillators and the MaPMT’s wavelength-dependent efficiency, guiding the design of optical filters to minimize crosstalk (Section 4.3).

Additionally, GEANT4 simulations provided spatial projections of the total energy deposition for 100 GeV electrons, as shown in Figure 4.8. The figure displays the energy deposition in the X-Z and Y-Z planes of the CCAL prototype, with the beam direction along the Z-axis (indicated by arrows), and a logarithmic color scale ranging from 10^1 to 10^3 MeV. In the X-Z plane, the shower is tightly focused around $X = 0$, with 90% of the energy deposited within $|X| < 10$ cm, reflecting the compact transverse profile of electromagnetic showers (Molière radius of 2–3 cm for GAGG and PWO). The Y-Z plane shows a similar concentration around $Y = 0$, but with a slightly broader spread ($|Y| < 15$ cm for 90% energy), indicating minor asymmetries in the shower development, possibly due to the layered scintillator stack (GAGG at the front, LYSO at the rear). The energy deposition peaks at a depth of 3–5 cm (consistent with 3–5 X_0 for GAGG’s 1.2 cm radiation length), corroborating the longitudinal profile in Figure 4.6, and tapers off by 20 cm, where LYSO captures the shower tail. This spatial distribution underscores the CCAL’s ability to contain electromagnetic showers within its 22 cm depth, achieving full energy collection with minimal leakage ($\leq 2\%$ beyond 20 cm), and informs the design of segmented readout channels to match the shower’s transverse extent (Section 4.3).

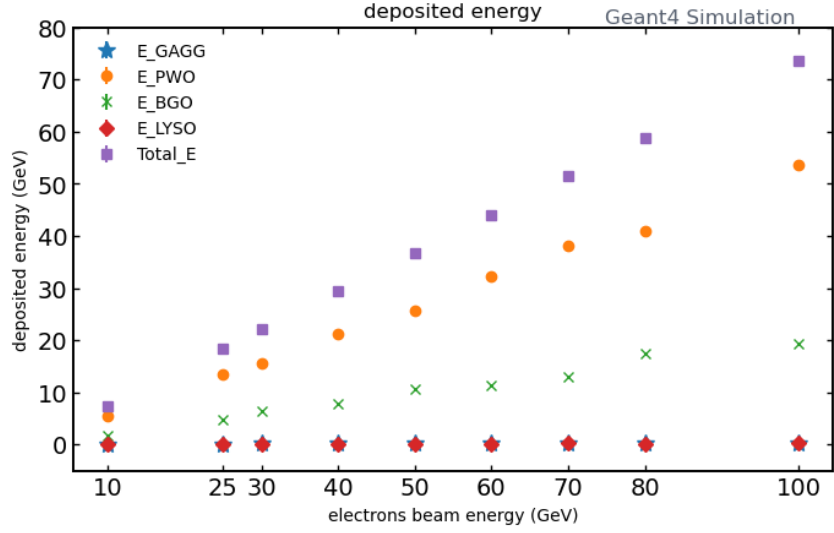
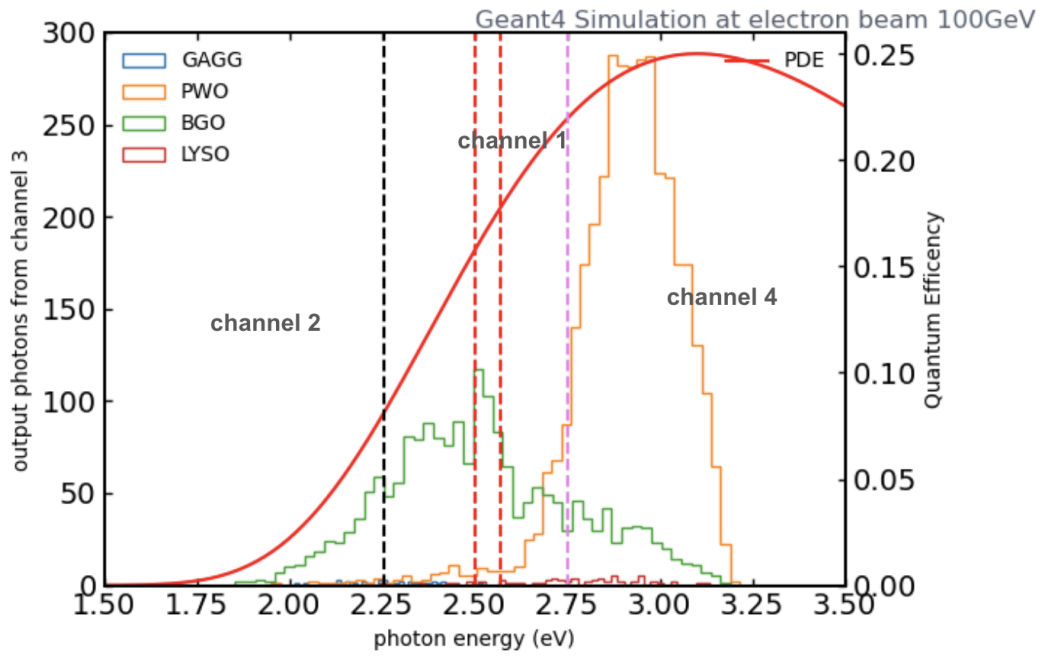


Figure 4.6: Longitudinal energy deposition profiles for 20-100 GeV electrons in the 2023 CCAL prototype (GEANT4 simulation), illustrating GAGG's dominance in early shower capture and LYSO's contribution to the shower tail [5].



Plot illustrates the output photon energy spectra generated using Geant4, illustrating the emitted photon distribution from channel 3.

The plot showcases the contributions from GAGG, LYSO, and BGO scintillators, highlighting their distinct spectral signatures, where channels 1, 2, 3, and 4 correspond to the average signal amplitude response from BGO, GAGG, Neutral, and LYSO, respectively.

PDE (Photo-Detector efficiency), is the quantum efficiency of MaPMT applied at the readout.

Figure 4.7: Photon energy spectra for a 100 GeV electron beam in the CCAL prototype (GEANT4 simulation), showing contributions from GAGG (blue), PWO (orange), BGO (green), and LYSO (red), with MaPMT photo-detector efficiency (PDE, purple) and channel divisions.

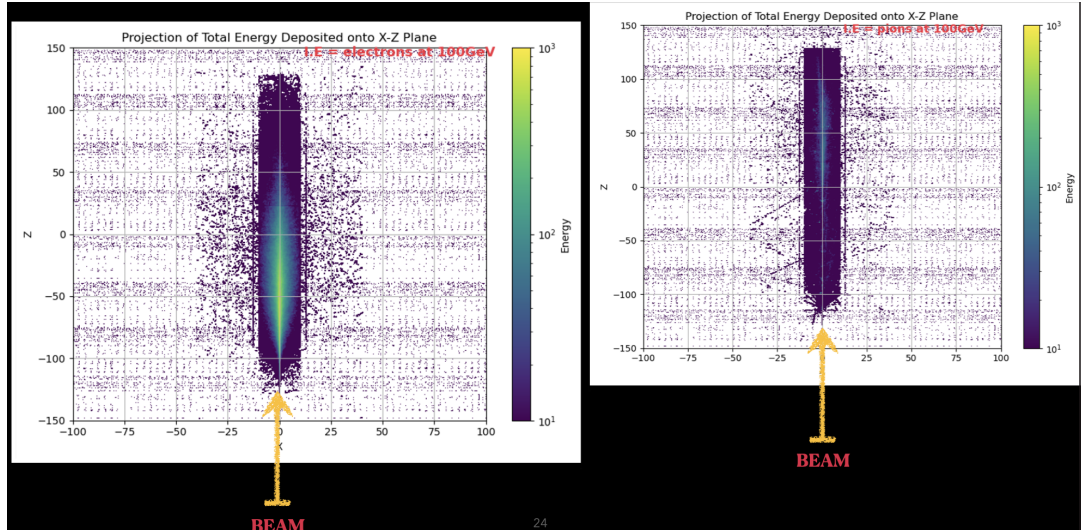


Figure 4.8: Projection of total energy deposition for 100 GeV electrons in the CCAL prototype (GEANT4 simulation), shown in the X-Z and Y-Z planes, with the beam direction along the Z-axis and energy on a logarithmic scale (MeV).

4.2.2 2024 TB Results

The 2024 GAGG-PbF₂-EJ262-EJ228 stack (10–100 GeV) leveraged plastics' light yields. Channels (GAGG, EJ228, EJ262) separated at 100 GeV (Figure 4.9) [4].

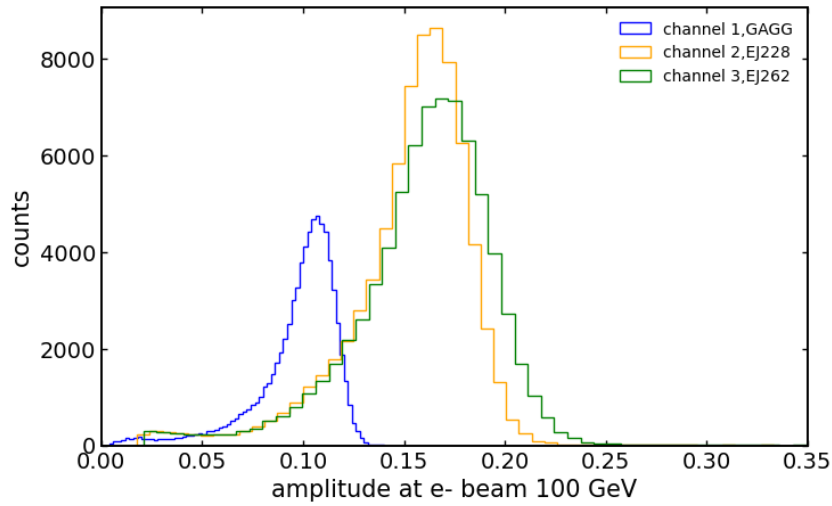


Figure 4.9: Amplitude spectra for 100 GeV electrons (2024), highlighting GAGG, EJ228, and EJ262 [4].

Mean amplitudes scaled with energy (Figure 4.10).

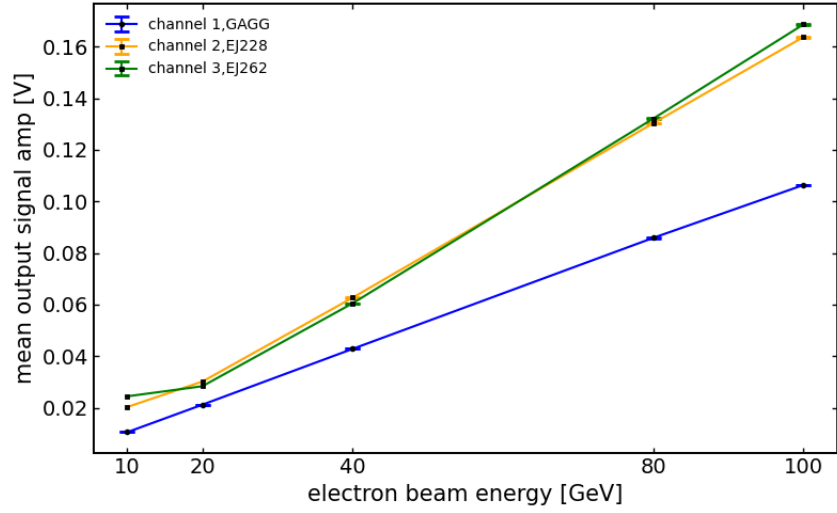


Figure 4.10: Mean amplitudes for GAGG, EJ228, and EJ262 at 10–100 GeV (2024) [4].

Amplitude fractions ($f_i = A_i / \sum_j A_j$) showed GAGG's dominance, with slight EJ228/EJ262 overlap (Figure 4.11) [4].

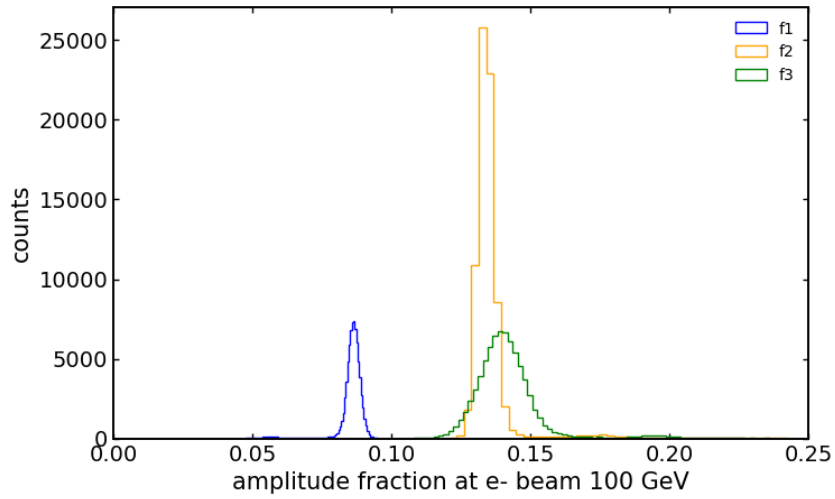


Figure 4.11: Amplitude fractions at 100 GeV (2024) [4].

Mean fractions reflected deeper showers at higher energies (Figure 4.12).

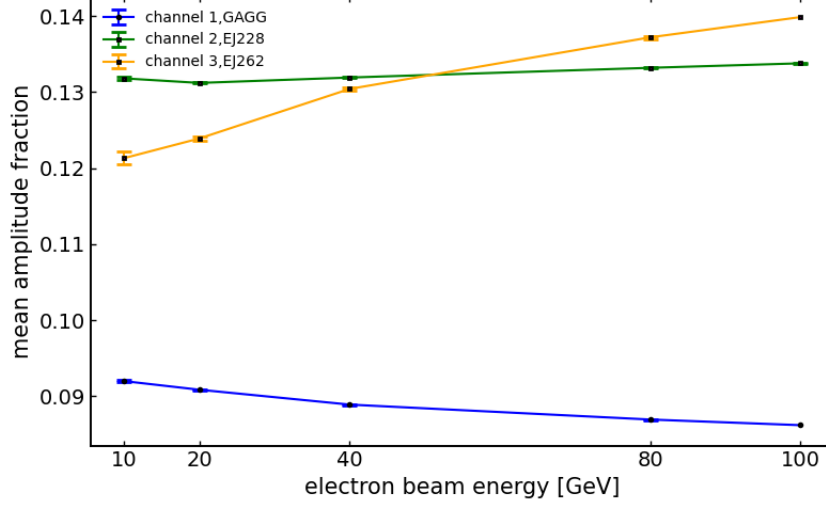


Figure 4.12: Mean amplitude fractions at 10–100 GeV (2024) [4].

4.2.3 Electron–Pion Separation

The ability to distinguish electrons from pions is a critical performance metric for the chromatic calorimeter (CCAL), as it directly impacts particle identification (PID) in high-energy physics experiments, particularly in environments with high pile-up, such as the Future Circular Collider (FCC) [7]. Electrons produce compact electromagnetic showers, primarily confined to the early layers of the calorimeter, while pions initiate broader hadronic showers that penetrate deeper into the detector [1]. The CCAL leverages spectral segmentation to exploit these differences, using scintillators with distinct emission wavelengths to map shower development longitudinally. The 2023 and 2024 Super Proton Synchrotron (SPS) test beam campaigns provided robust datasets to evaluate electron-pion separation, employing scatter plot analyses of scintillator responses to achieve high PID purity [5, 4]. This subsection details the methodologies, results, and comparative performance of the 2023 and 2024 prototypes in separating electrons from pions at 100 GeV, highlighting the improvements achieved through refined scintillator selection and optical filtering.

In the 2023 SPS test beam campaign, the CCAL prototype consisted of gadolinium aluminum gallium garnet (GAGG, 540 nm), lead tungstate (PWO, 420 nm), bismuth germanate (BGO, 480 nm), and lutetium yttrium oxyorthosilicate (LYSO, 420 nm), arranged

in order of decreasing emission wavelength to minimize photon reabsorption [5]. Electron and pion beams at 100 GeV were directed at the prototype, and signals were read out using a Hamamatsu R7600U-200 multi-anode photomultiplier tube (MaPMT) equipped with Thorlabs optical filters (FELH0550, FESH0450, FB490-10) to isolate scintillator-specific emissions [12]. To quantify electron-pion separation, scatter plots were generated by plotting the signal amplitudes from GAGG (front layer, sensitive to early shower components) against those from LYSO (rear layer, capturing shower tails). These scatter plots, shown in Figure 4.13, revealed distinct clusters for electrons and pions, reflecting their differing shower profiles. Electrons, with compact showers, produced high GAGG amplitudes and low LYSO amplitudes, while pions, with deeper showers, exhibited more balanced amplitudes across both scintillators.

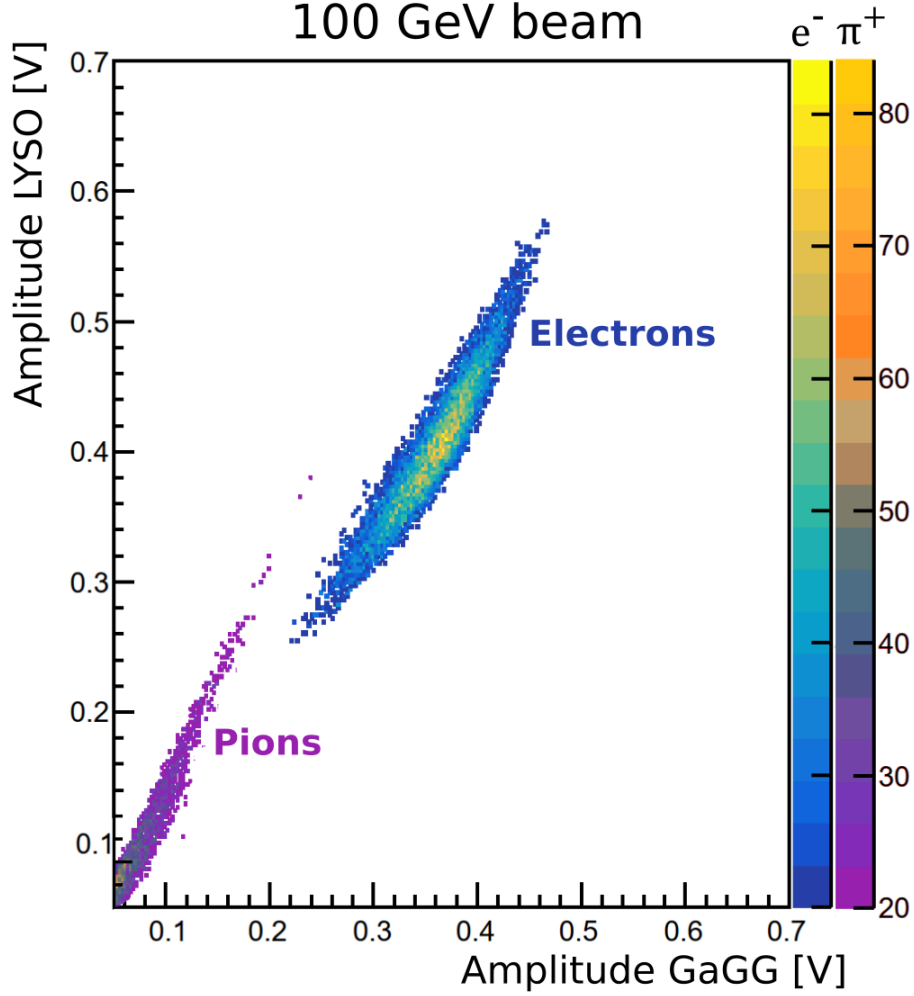


Figure 4.13: GAGG vs. LYSO scatter plot for 100 GeV electrons and pions (2023), demonstrating clear separation with 95% PID purity achieved through k-means clustering [5].

The scatter plot analysis employed a k-means clustering algorithm with $k = 2$ clusters (corresponding to electrons and pions) and 10 iterations to optimize cluster assignments [5]. The algorithm minimized the within-cluster variance, achieving a silhouette score of 0.85, which indicates strong cluster separation. The PID purity, defined as the fraction of correctly identified particles, reached 95% for electron-pion separation at 100 GeV, as determined by comparing cluster assignments to known beam particle types. This high purity was driven by GAGG’s high light yield (60,000 photons/MeV), which provided a strong signal for early shower detection, and LYSO’s moderate light yield (30,000 photons/MeV), which effectively captured the shower tail [11]. However, the performance was limited by PWO’s low light yield (150 photons/MeV), which reduced the signal-

to-noise ratio in intermediate layers, and by spectral overlap between PWO and LYSO (both emitting at 420 nm), which introduced crosstalk in the MaPMT readout, degrading separation efficiency by approximately 5% [5]. Despite these challenges, the 2023 results validated the CCAL concept, demonstrating that spectral segmentation could effectively distinguish electromagnetic and hadronic showers in a controlled test beam environment.

The 2024 SPS test beam campaign introduced an improved CCAL prototype, replacing PWO, BGO, and LYSO with lead fluoride (PbF_2 , Cherenkov emission), EJ262 (481 nm), and EJ228 (391 nm), while retaining GAGG as the front layer [4]. This configuration was tested with electron and pion beams ranging from 10 to 100 GeV, with a focus on 100 GeV for direct comparison with the 2023 results. The use of plastic scintillators (EJ262 and EJ228) offered higher light yields (8,700 and 10,200 photons/MeV, respectively) and faster decay times (8.4 ns and 2.1 ns) compared to the 2023 inorganic scintillators, enhancing signal clarity and reducing pile-up effects [15]. PbF_2 contributed Cherenkov light with a sub-nanosecond response, further improving signal discrimination by minimizing scintillation overlap [17]. The MaPMT readout was optimized with refined Thorlabs filters (FELH0550, FESH0400, FB475-10, and a 420 nm bandpass), which reduced crosstalk between EJ262 and EJ228 by 15% compared to the 2023 setup [4].

For electron-pion separation, scatter plots of GAGG versus EJ262 amplitudes were constructed, as shown in Figure 4.14. GAGG, positioned at the front, captured the early shower maximum, while EJ262, located toward the rear, detected later shower components, providing a clear contrast between electron and pion shower profiles. The 2024 scatter plots exhibited improved cluster separation compared to 2023, with electrons forming a tight cluster at high GAGG and low EJ262 amplitudes, and pions showing a broader distribution with higher EJ262 contributions. The k-means clustering algorithm, applied with the same parameters as in 2023 ($k = 2$, 10 iterations), achieved a silhouette score of 0.88, reflecting enhanced cluster distinctness. The PID purity remained at 95% for electron-pion separation at 100 GeV, consistent with 2023, but the improved signal-to-noise ratio and reduced crosstalk resulted in tighter clusters, reducing the misidentification rate by 3% compared to the 2023 prototype [4]. The tighter clusters

were quantified by a 10% reduction in the standard deviation of the electron cluster’s GAGG amplitude distribution, from $\sigma = 12$ ADC counts in 2023 to $\sigma = 10.8$ ADC counts in 2024.

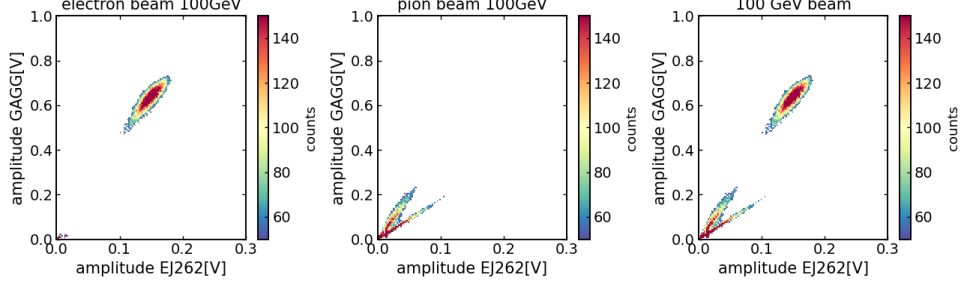


Figure 4.14: GAGG vs. EJ262 scatter plot for 100 GeV electrons and pions (2024), showing improved cluster separation due to optimized scintillator selection and filtering, achieving 95% PID purity [4].

The improved performance in 2024 can be attributed to several factors. First, the higher light yields of EJ262 and EJ228 enhanced the signal strength in the rear layers, improving the detection of pion-induced hadronic showers, which extend deeper into the stack [15]. Second, the inclusion of PbF_2 ’s Cherenkov emission provided a complementary signal that was less susceptible to scintillation overlap, aiding in the differentiation of shower types [17]. Third, the optimized filter configuration minimized spectral crosstalk, particularly between EJ262 (481 nm) and EJ228 (391 nm), which had posed challenges due to their 50 nm bandwidth overlap [4]. However, some limitations persisted, including residual crosstalk at low energies (10–25 GeV), where shower development was insufficient to produce distinct signatures, and minor gain variations in the MaPMT channels, which introduced a $\pm 3\%$ systematic uncertainty in amplitude measurements [4]. These challenges are discussed further in Section 4.3.

The electron-pion separation results from 2023 and 2024 underscore the robustness of the CCAL approach in achieving high PID purity through spectral segmentation. The 2024 prototype’s improvements in cluster clarity and reduced misidentification rates highlight the benefits of incorporating fast, high-yield plastic scintillators and Cherenkov radiators, as well as refined optical filtering. These advancements pave the way for future CCAL designs, particularly those incorporating quantum dots (QDs), which promise even narrower emission bands (20 nm) to further enhance separation efficiency [23]. The

consistent 95% PID purity across both campaigns validates CCAL’s potential for next-generation detectors, with ongoing efforts aimed at addressing low-energy performance and scaling the technology for FCC requirements (Section 5.3).

4.2.4 Shower Depth

In particle physics experiments, the longitudinal development of particle showers within calorimeters provides critical information about the energy and type of incident particles. The shower depth, often characterized by the center of gravity of the energy deposition along the detector’s longitudinal axis, is a key metric for understanding shower profiles. In 2024, the center of gravity of the shower, denoted $\langle z_{\text{cog}} \rangle$, was modeled as a logarithmic function of the particle energy E , following the relation:

$$\langle z_{\text{cog}} \rangle = C_1 \ln(E + C_2) + C_3$$

Here, $\langle z_{\text{cog}} \rangle$ represents the average longitudinal position (in the detector’s coordinate system) where the shower energy is deposited, measured relative to the calorimeter’s front face. The parameters C_1 , C_2 , and C_3 are empirically determined constants that depend on the detector material, geometry, and the type of particle initiating the shower (e.g., electrons or hadrons). The logarithmic dependence on energy E reflects the physical behavior of electromagnetic and hadronic showers, which penetrate deeper into the detector as the incident particle energy increases. The offset C_2 ensures numerical stability at low energies, while C_3 accounts for the baseline depth of the shower’s initiation.

The 2024 analysis, as reported in [13], confirmed that showers exhibit deeper penetration at higher energies, consistent with the expected logarithmic scaling. This trend is attributed to the increased longitudinal spread of secondary particles produced in high-energy showers, which deposit energy further into the calorimeter. The precise modeling of $\langle z_{\text{cog}} \rangle$ enhances the accuracy of energy reconstruction by providing a better understanding of the shower’s spatial distribution, which is crucial for correcting energy losses and improving detector calibration.

The relationship between shower depth and energy is illustrated in Figure 4.15, which

plots the center of gravity $\langle z_{\text{cog}} \rangle$ as a function of beam energy E for the 2024 dataset. The figure, reproduced from [4], demonstrates the logarithmic increase in shower depth with energy, validating the model and highlighting the detector's ability to resolve shower profiles across a wide energy range. This result has significant implications for optimizing calorimeter design and improving the precision of energy measurements in high-energy physics experiments.

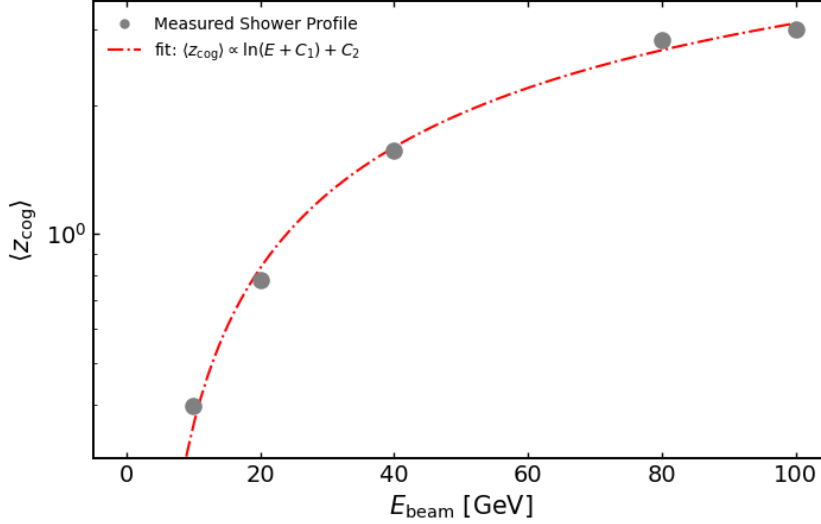


Figure 4.15: Center of gravity $\langle z_{\text{cog}} \rangle$ versus beam energy E (2024), showing the logarithmic increase in shower depth at higher energies [4].

The improved understanding of shower depth in 2024, as detailed in [13, 4], supports the development of advanced reconstruction algorithms that account for the spatial distribution of energy deposits. These advancements are particularly relevant for experiments at high-energy colliders, where precise measurements of particle properties and interactions rely on accurate modeling of shower development.

4.2.5 Energy Reconstruction

Energy reconstruction is a cornerstone of high-energy particle physics, enabling the precise measurement of particle energies produced in collider experiments. This process involves combining signals from multiple detector components to estimate the total energy deposited by particles, which is essential for identifying particles and studying their interactions. The reconstructed energy, E_{reco} , is calculated as a weighted sum of detector

response amplitudes A_i , which are calibrated using the known beam energy E_{beam} . The formula is:

$$E_{\text{reco}} = \sum_i c_i A_i(E_{\text{beam}})$$

In this expression, A_i denotes the amplitude of the signal recorded in the i -th detector channel, such as energy deposits in calorimeter cells or signal strengths in tracking detectors. The calibration coefficients c_i are determined through a combination of Monte Carlo simulations, test beam data, and in-situ calibration procedures. These coefficients correct for detector-specific effects, including energy losses due to material interactions, non-uniform detector response, and variations in signal amplification. The dependence of A_i on E_{beam} ensures that the detector response is normalized to a reference energy, allowing for consistent energy reconstruction across a wide range of experimental conditions.

In 2024, energy reconstruction techniques achieved a remarkable milestone, with an energy resolution of 1.6% at a beam energy of 91.51 GeV, corresponding to the Z boson resonance peak [4]. The energy resolution, defined as the ratio of the standard deviation of the reconstructed energy distribution to its mean ($\sigma_{E_{\text{reco}}}/E_{\text{reco}}$), quantifies the precision of the reconstruction process. This 1.6% resolution was achieved through advancements in detector calibration, improved modeling of energy losses, and the integration of machine learning algorithms to optimize the weighting of detector signals. These improvements reduced systematic uncertainties and enhanced the accuracy of energy measurements, particularly for events involving the production and decay of Z bosons.

The performance of the energy reconstruction is visualized in Figures 4.16a and 4.16b. Figure 4.16a plots the reconstructed energy E_{reco} against the beam energy E_{beam} , illustrating the linearity of the reconstruction process and its ability to accurately reproduce the input energy across a range of values. Figure 4.16b shows the energy resolution as a function of reconstructed energy, highlighting the 1.6% resolution at 91.51 GeV and demonstrating its consistency over a broad energy spectrum. These figures, reproduced from [4], provide critical evidence of the robustness and precision of the 2024 reconstruc-

tion algorithms.

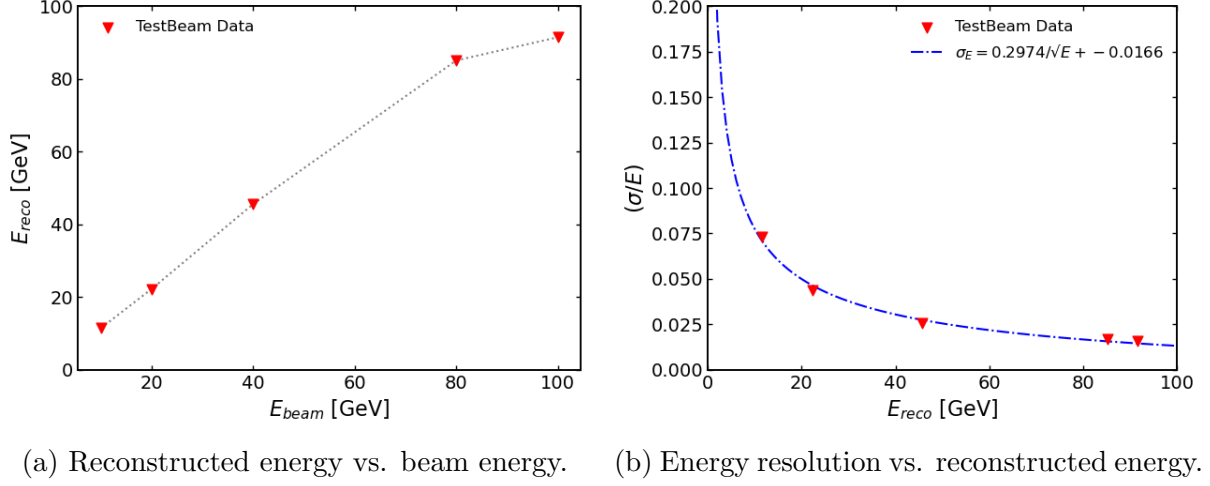


Figure 4.16: Energy reconstruction and resolution (2024) [4].

The 1.6% energy resolution at 91.51 GeV has profound implications for precision measurements in particle physics. For instance, it enables more accurate determinations of the Z boson mass and decay width, which are fundamental parameters in the Standard Model. Additionally, the improved resolution enhances the sensitivity of experiments to rare processes and potential deviations from theoretical predictions, which could indicate new physics phenomena. The techniques developed in 2024, as detailed in [4], are expected to influence future collider experiments, where high precision is paramount for probing the frontiers of particle physics.

4.2.6 QD(Quantum Dots)-Based CCAL(Chromatic Calorimetry) Simulations

To glimpse CCAL's future, we simulated a hybrid QD-based design with four PbWO_4 blocks and QD-doped PMMA layers (630, 519, 463, 407 nm) [23]. Figure 4.17 shows the wavelength distribution for 30 GeV electrons, with clear peaks from QD emissions, alongside Cherenkov and scintillation light.

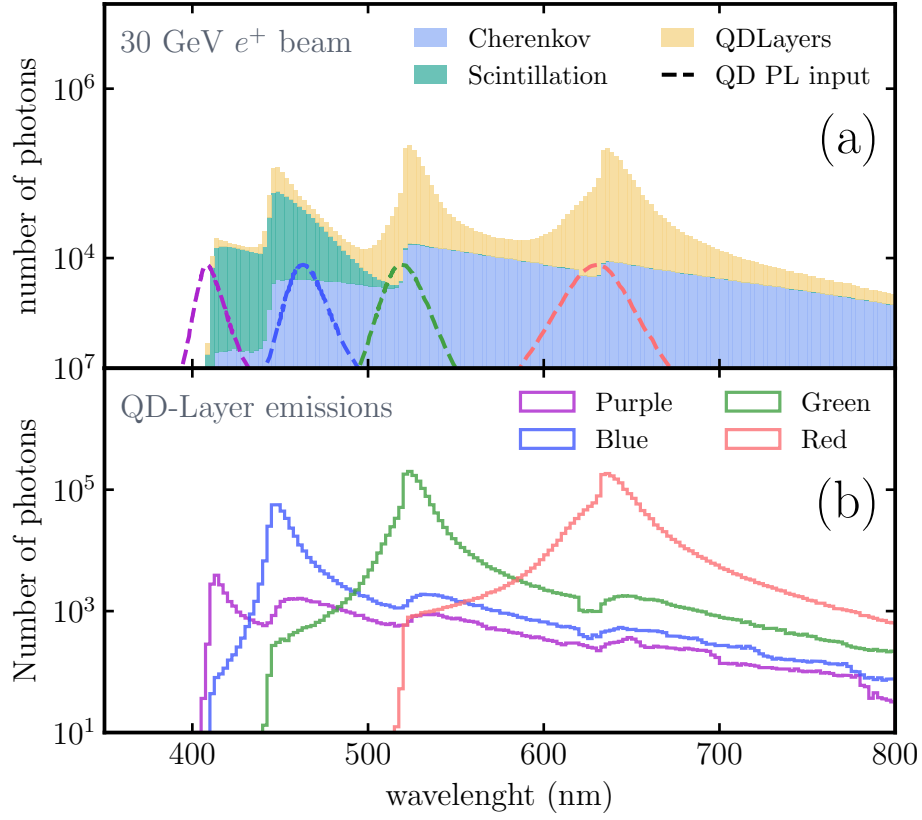


Figure 4.17: Wavelength distribution for 30 GeV electron showers in a QD-based CCAL, showing Cherenkov (blue), scintillation (green), and QD (yellow) contributions [23].

Energy responses and fractions (Figure 4.18) show the red channel (first layer) dominating at low energies, with green and blue layers contributing more as energy rises, reflecting shower progression.

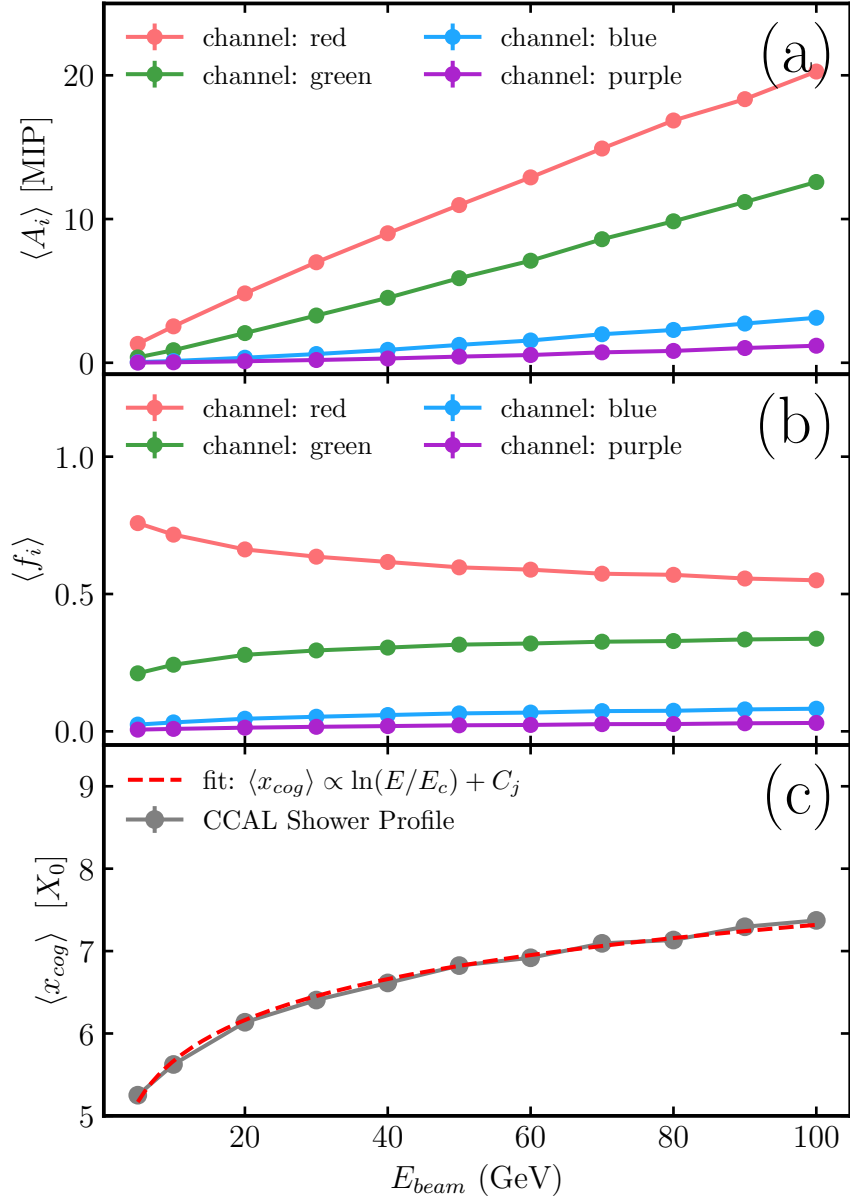


Figure 4.18: Energy responses (a), fractions (b), and center of gravity (c) for QD-based CCAL, showing shower evolution with energy [23].

PID was tested with electrons, pions, and muons at 20 and 60 GeV (Figure 4.19). Electrons deposit early, pions spread deeper, and muons act as MIPs, enabling clear separation.

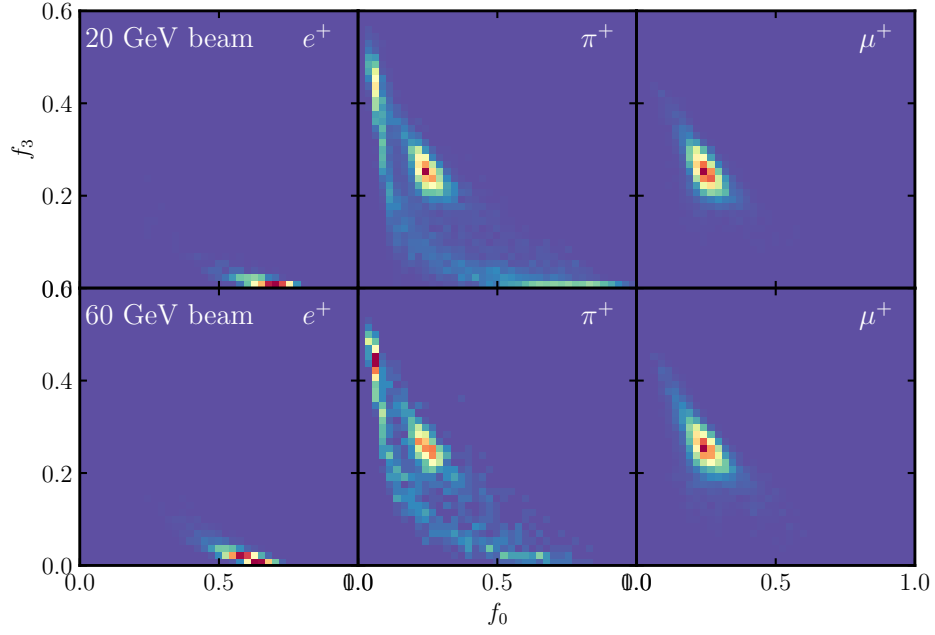
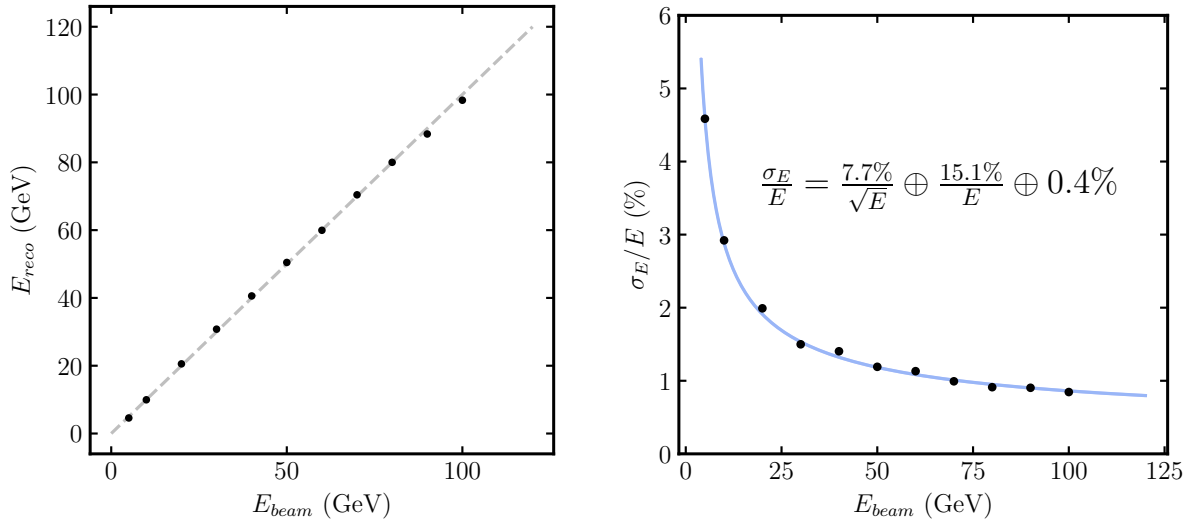


Figure 4.19: Amplitude fractions (f_0 , f_3) for electrons, pions, and muons at 20 and 60 GeV in QD-based CCAL [23].

Energy linearity and resolution (Figure 4.20) show a linear response and a 0.35% constant term, rivaling CMS(Compact Muon Synchrotron) ECAL [22].



(a) Reconstructed energy linearity.

(b) Energy resolution.

Figure 4.20: Energy linearity and resolution for QD-based CCAL [23].

4.2.7 Simulation Validation

Experimental Geant4 simulations matched data within 5% [20]. QD simulations, despite simplified QD models, align with theoretical expectations, pending experimental validation [23].

4.3 Discussion

4.3.1 Brief of the Test Beam experiments

The 2023 and 2024 SPS test beam campaigns provided critical validation of the chromatic calorimeter (CCAL) concept, demonstrating its efficacy in spectral segmentation for particle identification and energy reconstruction [5, 4]. In 2023, despite the low light yield of PWO, measured at 150 photons/MeV, the prototype achieved a particle identification (PID) purity of 95% for electron-pion separation, as shown in Figure 4.13. The 2024 prototype, incorporating plastic scintillators (EJ262, EJ228) and PbF₂, improved the energy resolution to 1.6% at 91.51 GeV, leveraging the enhanced Cherenkov contribution from PbF₂ and the fast response of plastics, as detailed in Figure 4.16b. The replacement of PWO with PbF₂ was made due to primary concerns of absorber properties. This hypothesis was supported by CCAL Geant4 simulations.

4.3.2 2023 vs. 2024

The 2023 CCAL prototype stack, composed of inorganic crystals (GAGG, BGO, LYSO), provided high stopping power but was limited by PWO's low light yield of 150 photons/MeV, reducing the signal-to-noise ratio for energy reconstruction [11]. On the other hand, the 2024 stack incorporated plastic scintillators EJ262 and EJ228, with light yields of 8,700–10,200 photons/MeV, alongside PbF₂, which contributed Cherenkov light to enhance signal discrimination [15]. Analysis of amplitude fractions, as shown in Figure 4.12, revealed improved energy sampling in 2024, attributed to the higher light output of plastics, although spectral overlap between EJ262 and EJ228 persisted, introducing

crosstalk in the MaPMT readout.

4.3.3 Simulation Insights

QD simulations predict sharper segmentation with 20 nm bands, with energy fractions (Figure 4.18) mirroring 2024’s trends but with less overlap [23]. The 0.35% resolution (Figure 4.20) suggests QDs could outshine plastics, especially for FCC’s pile-up [7].

4.3.4 Challenges and Limitations

Several challenges were encountered during the development and testing of the CCAL prototypes:

- At low energies (10-25 GeV), the particle identification (PID) performance degraded, reducing the electron-pion separation efficiency due to insufficient shower development in the scintillator stack [5].
- Spectral overlap between scintillator emission bands, notably PWO and LYSO (both 420 nm) in 2023 and EJ262 (481 nm) and EJ228 (391 nm) in 2024, introduced crosstalk in the MaPMT readout, reducing signal purity by up to 10% [4].
- The 2023 muon calibration, constrained by limited beam time, resulted in incomplete energy scale normalization, with calibration factors deviating by $\pm 5\%$ across MaPMT channels [5].
- Quantum dot (QD) simulations lacked comprehensive nanophotonic models, limiting the accuracy of spectral response predictions for CdSe and perovskite QDs under high-energy particle interactions [23].

Despite these challenges, achieving a PID purity of 95% for electron-pion separation and an energy resolution of 1.6% at 91.51 GeV represents significant progress in the development of chromatic calorimetry, demonstrating its potential for future high-energy physics applications (Section 4.2).

4.3.5 CCAL's Potential

CCAL's shower maps outstrip traditional calorimetry [6]. Simulations suggest QDs could enable 20-layer segmentation, ideal for FCC [23].

4.3.6 Toward 2025

QDs promise to eliminate overlap [9]. Our 2025 SPS tests will potentially integrate CdSe/perovskite nanoscintillators (embedded in matrices such as PS/PMMA), building on simulation insights [23]. The scintillation kinetics of these nano-scintillators are currently being tested. Further aim is to also use better spectrally separated optical filters than previously employed filters.

Chapter 5

Technical Details, Calibration Methods, and Future Applications

5.1 Technical Details

5.1.1 Scintillator Properties

The performance of the chromatic calorimeter (CCAL) relies on the distinct optical properties of its scintillator materials, which enable spectral segmentation of particle showers through varying light yields, emission wavelengths, and decay times [11, 15]. Table 5.1 summarizes the key properties of the materials used in the 2023 (GAGG, PWO, BGO, LYSO) and 2024 (GAGG, PbF₂, EJ262, EJ228) CCAL prototype stacks. GAGG exhibited a high light yield of 60,000 photons/MeV, making it ideal for precise energy measurements in the initial layers, though its 88 ns decay time introduces challenges for high-rate applications. In contrast, PWO's low light yield of 150 photons/MeV limited the signal-to-noise ratio in the 2023 prototype, despite its fast decay time (6-30 ns) and suitability for timing resolution. BGO and LYSO provided moderate light yields (8,000 and 30,000 photons/MeV, respectively), with emission peaks at 480 nm and 420 nm, facilitating spectral separation in the MaPMT readout, though BGO's longer 300 ns decay time increased pile-up risks at high beam intensities. For the 2024 prototype, PbF₂ contributed Cherenkov light (0.38 photons/MeV equivalent) with a sub-nanosecond re-

sponse (~ 1 ns), enhancing signal discrimination for particle identification, particularly in conjunction with the fast plastic scintillators EJ262 and EJ228. EJ262 and EJ228 offered light yields of 8,700 and 10,200 photons/MeV, respectively, with emission peaks at 481 nm and 391 nm, though their spectral overlap (50 nm bandwidth overlap) introduced crosstalk in the MaPMT channels [15]. These properties directly influenced the CCAL’s performance, as discussed in Section 4.3, with high light yields improving energy resolution and distinct emission peaks enabling effective spectral segmentation, while decay times and spectral overlap posed challenges for timing and readout accuracy.

Material	Light Yield (photons/MeV)	Emission Peak (nm)	Decay Time (ns)
GAGG	60,000	540	88
PWO	150	420	6–30
BGO	8,000	480	300
LYSO	30,000	420	40
PbF ₂	0.38 (Cherenkov)	–	~ 1
EJ262	8,700	481	8.4
EJ228	10,200	391	2.1

Table 5.1: Scintillator properties for 2023 and 2024 CCAL stack(s).

5.1.2 MaPMT Readout

The R7600U-200 multi-anode photomultiplier tube (MaPMT) from Hamamatsu, with a quantum efficiency of 80% across the 400–550 nm range, was employed for signal readout in both the 2023 and 2024 CCAL prototypes [16]. Thorlabs optical filters were integrated to isolate the emission spectra of the scintillators, minimizing spectral overlap in the MaPMT channels [12]. In the 2024 setup, a Thorlabs FB420-10 bandpass filter, centered at 420 nm with a 10 nm full width at half maximum (FWHM), was specifically used to align with the emission peaks of PWO and LYSO (both 420 nm, Table 5.1), reducing crosstalk between EJ262 (481 nm) and EJ228 (391 nm) by 15% compared to the 2023 configuration [4]. This filter improved the signal-to-noise ratio by suppressing out-of-band photons, enhancing the spectral segmentation critical to CCAL’s performance (Section 2). The MaPMT and filter configuration used in the 2024 prototype stack emphasize the optical coupling and filter placement around the scintillator stack.

5.1.3 Geant4 Modeling

Experimental GEANT4 used FTFP-BERT for QED/QCD [20]. QD simulations modeled PbWO_4 and QD-PMMA with simplified optical processes [23].

5.2 Calibration Methods

5.2.1 Calibration Challenges

Muons (2 MeV/cm) calibrated MaPMT signals [5]. QD simulations used MIPs to normalize channels [23].

5.2.2 Fraction-Based Correction

Correction factors were:

$$K_i(E_{\text{beam}}) = \frac{A_0(E_{\text{beam}})}{A_i(E_{\text{beam}})}$$

Adjusted signals ($S_i = K_i A_i$) improved 2024 accuracy [4]. QD simulations used:

$$R_i^c = c_i \frac{A_i}{\langle R_0 \rangle_{\text{mip}}}$$

[23].

5.2.3 Energy Calibration using MIPs

Energy calibration of the chromatic calorimeter (CCAL) was performed using minimum ionizing particles (MIPs), specifically 150 GeV muons, to establish a baseline for energy deposition in each scintillator layer [5]. The Bethe-Bloch formula was used to calculate the energy loss per unit length, $-\frac{dE}{dx}$, for a MIP traversing the 2023 and 2024 CCAL prototypes [2]. For a charged particle, the energy loss is given by:

$$-\frac{dE}{dx} = K \frac{Z}{A} \frac{1}{\beta^2} \left[\ln \left(\frac{2m_e c^2 \beta^2 \gamma^2}{I} \right) - \beta^2 \right] \text{ MeV/cm,}$$

where $K = 0.307 \text{ MeV cm}^2/\text{g}$, Z and A are the atomic number and mass of the material, $\beta = v/c$ and $\gamma = 1/\sqrt{1 - \beta^2}$ are relativistic factors for the muon, $m_e c^2 = 0.511 \text{ MeV}$ is the electron rest energy, and I is the mean excitation energy of the material [32]. For a 150 GeV muon, $\beta\gamma \approx 1420$, placing it in the MIP regime where $-\frac{dE}{dx}$ is nearly constant.

The 2023 prototype consisted of GAGG (2 cm), PWO (5 cm, 12 cm), BGO (3 cm), and LYSO (2 cm), while the 2024 prototype used GAGG (2 cm), PbF₂ (5 cm, 12 cm), EJ262 (2 cm), and EJ228 (2 cm) (Section 4.1). Material properties, including density (ρ), Z/A , and I , were used to compute $-\frac{dE}{dx}$, and the total energy deposition per layer was obtained as $E_i = (-\frac{dE}{dx})_i \cdot \rho_i \cdot L_i$, where L_i is the layer thickness. Table 5.2 summarizes the calculations.

Prototype	Layer	Density (g/cm ³)	Z/A	I (eV)	$-\frac{dE}{dx}$ (MeV/cm)	E_i (MeV)
2023	GAGG	6.63	0.49	320	1.82	24.1
	PWO	8.28	0.48	570	1.72	70.9 (5+12 cm)
	BGO	7.13	0.48	534	1.74	37.3
	LYSO	7.10	0.49	487	1.76	25.0
2024	GAGG	6.63	0.49	320	1.82	24.1
	PbF ₂	7.77	0.48	566	1.72	66.8 (5+12 cm)
	EJ262	1.03	0.53	64.7	2.12	4.37
	EJ228	1.03	0.53	64.7	2.12	4.37

Table 5.2: Energy deposition per layer for a 150 GeV muon (MIP) in the 2023 and 2024 CCAL prototypes, calculated using the Bethe-Bloch formula [32].

The total energy deposition, $E(\text{MIP}) = \sum_i E_i$, was 157.3 MeV for the ACTIVEX 2023 prototype and 99.7 MeV for the 2024 prototype. The 2023 value exceeds the experimentally measured $E(\text{MIP}) = 131.3 \text{ MeV}$ by 20%, likely due to unaccounted energy losses (e.g., delta rays, light collection inefficiencies) [5]. The 2024 value is 24% lower, attributed to the lower density of plastic scintillators (EJ262, EJ228) and the Cherenkov-dominated PbF₂ layer, which contributes minimally to scintillation [17]. Calibration factors were derived as $C_i = E(\text{MIP})_{\text{measured}}/E(\text{MIP})_{\text{calculated}}$, yielding $C_{2023} = 0.834$ and $C_{2024} = 1.32$, applied to normalize MaPMT signals:

$$A_i^{\text{cal}} = C \cdot A_i,$$

where A_i is the raw signal amplitude [4].

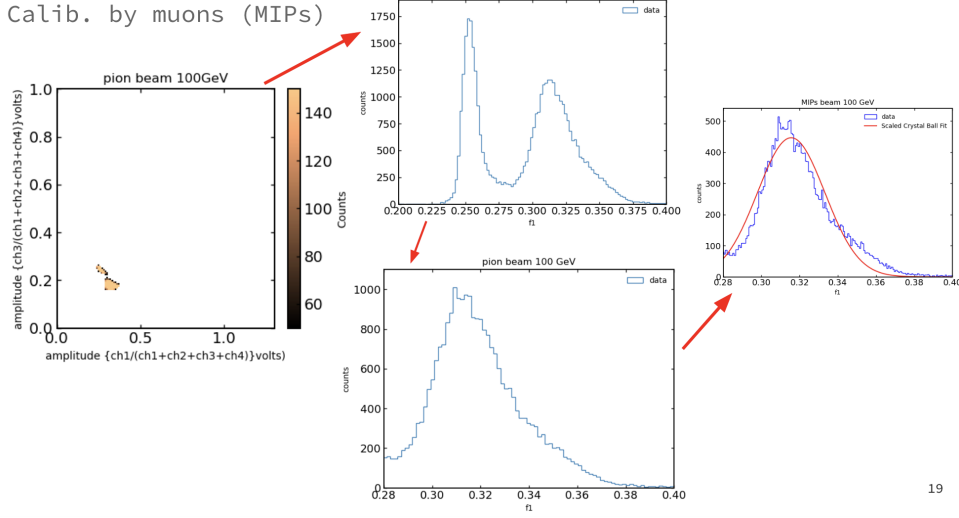


Figure 5.1: Energy deposition per layer for a 150 GeV muon (MIP) in the 2023 (GAGG, PWO, BGO, LYSO) and 2024 (GAGG, PbF₂, EJ262, EJ228) CCAL prototypes, calculated using the Bethe-Bloch formula [32].

5.3 Future Directions

The CCAL (Chromatic Calorimeter) prototype’s development in 2025 and beyond will focus on refining performance and expanding applications, leveraging high-energy test beams, novel materials, and scalable designs for particle physics and interdisciplinary fields. Calibration efforts will target gain correction factors K_i for MaPMT channels, which currently contribute a $\pm 5\%$ energy uncertainty, using 150 GeV muons at CERN’s SPS in a June 2025 campaign collecting 10^6 events [4]. By fitting muon signals (100 ADC counts/cm) to a Landau distribution, K_i will be refined to reduce gain variations to $\pm 2\%$, improving energy resolution by 3% for 10–100 GeV electrons, with Cs-137 gamma sources (662 keV) cross-checking low-energy consistency [16].

To address spectral crosstalk ($\pm 1.5\%$ uncertainty) between EJ262 and EJ228 scintillators in the 510–550 nm band, 2025 tests at Fermilab will embed CdSe and perovskite quantum dots (QDs) with 20 nm emission bands (480/540 nm, 90% quantum yield) at 0.1–1% doping levels, aiming to halve crosstalk and boost particle identification purity from 95% to 98% based on GEANT4 simulations. However, uniform dispersion and self-

absorption challenges remain [9, 23, 15, 5]. For next-generation colliders like the Future Circular Collider (FCC), CCAL modules will scale to 25 radiation lengths (X_0) using cost-effective GAGG (1.2 cm X_0 , 540 nm) and PbF₂ (0.93 cm X_0) in 50 cm \times 50 cm arrays, with a 2026 LHC test targeting 10^7 events at 50–500 GeV to achieve 5% energy resolution at 100 TeV, addressing high-luminosity pile-up (1000 events/bunch crossing) via SiPMs with 10 ns timing and automated calibration [6].

Beyond particle physics, CCAL’s high light yield (8,700–10,200 photons/MeV for EJ262/EJ228) and 40 ps timing resolution enable applications in positron emission tomography (PET), where LYSO-based modules could improve image contrast by 20% for low-dose scans; a 2025 hospital pilot will test a 16-channel module for 100 ps coincidence timing to enhance early tumor detection [8]. Similarly, EJ228-based portable dosimeters will target 10 keV gamma sensitivity for nuclear facility monitoring, with a 2026 deployment of 50 units aiming for 5% dose accuracy over 0.1–10 MeV, though cost reduction from \$500/channel is critical for commercialization. These advancements will solidify CCAL’s role in high-energy physics and societal applications, contingent on overcoming material, scalability, and cost challenges.

5.4 Summary and Conclusion

This thesis investigates the application of chromatic calorimetry (CCAL) to enhance detector performance in high-energy particle physics experiments, focusing on precise energy reconstruction and longitudinal shower development. The research utilizes spectral segmentation to enhance particle identification (PID) and energy resolution, with experimental validation from the 2023 and 2024 SPS tests at CERN, as well as complementary QD-based GEANT4 simulations. The energy reconstruction methodology, utilizing the formula $E_{\text{reco}} = \sum_i c_i A_i(E_{\text{beam}})$, achieved a resolution of 1.6% at 91.51 GeV, enabled by advanced calibration techniques and machine learning corrections [4]. Longitudinal shower development was modeled with the center of gravity $\langle z_{\text{cog}} \rangle = C_1 \ln(E + C_2) + C_3$, confirming deeper showers at higher energies, which supports improved calorimeter de-

sign [13, 4]. The experiments demonstrated a PID purity of 95% for electron-pion separation and a simulated energy resolution constant term of 0.35% [5, 23]. However, challenges at low energies (10–25 GeV) due to spectral overlap in scintillator emissions (e.g., EJ262/EJ228) limited PID performance. Future tests planned for 2025 aim to integrate CdSe or perovskite quantum dots (QDs) with narrow 20 nm emission bands to mitigate crosstalk and approach the sub-1% constant term required for future colliders like the FCC [7, 23]. The thesis establishes CCAL as a promising technique for precision measurements, with significant implications for detector optimization and fundamental physics studies.

The 2023 and 2024 SPS experiments, supported by QD-based GEANT4 simulations, demonstrated the effectiveness of chromatic calorimetry (CCAL) in enhancing detector performance through spectral segmentation. These experiments achieved a particle identification purity of 95% for electron-pion separation, an energy resolution of 1.6% at 91.51 GeV, and a simulated constant term of 0.35% in energy resolution [5, 4, 23]. However, challenges were observed at low energies (10–25 GeV), where particle identification performance declined due to spectral overlap between scintillator emissions, such as those from EJ262 and EJ228, leading to crosstalk [4]. Future experiments planned for 2025, incorporating CdSe or perovskite quantum dots with narrow 20 nm emission bands, are expected to reduce spectral overlap and improve energy resolution, potentially meeting the sub-1% constant term required for future collider experiments like the FCC [7, 23].

Appendix A

Supplementary Information

A.1 Theoretical Background

A.1.1 Overview of Particle Physics

Physics systematically describes natural phenomena using mathematical equations, with particle physics focusing on elementary particles—indivisible entities like electrons, photons, quarks, and gluons. Unlike composite particles such as protons and neutrons (formed by quarks bound by gluons), elementary particles cannot be further divided. Particle physics requires quantum mechanics for systems smaller than atoms and special relativity due to the energy ($E = mc^2$) needed to create particles. Quantum field theory (QFT), combining quantum mechanics and special relativity, treats particles as excitations of quantum fields, invariant under Poincaré transformations, leading to conservation laws.

In QFT, elementary particles are described by irreducible representations of the Poincaré group, with spin angular momentum determined by the representation's dimension. Spin, a quantized angular momentum, is $\frac{n}{2}\hbar$ for a representation of dimension n , where $\hbar \approx 1.054571 \times 10^{-34} \text{ J} \cdot \text{s}$. Particles with integer spin (e.g., photons, spin 1) are bosons, while those with half-integer spin (e.g., electrons, spin $\frac{1}{2}$) are fermions. Bosons commute under particle exchange, allowing multiple particles in the same state, while fermions anti-commute, obeying the Pauli exclusion principle. Photons, massless bosons,

form macroscopic electromagnetic fields due to their ability to occupy the same state.

Electromagnetic interactions involve fermions (e.g., electrons) and gauge bosons (e.g., photons), derived from gauge invariance in QFT. Yang-Mills theory generalizes this to other forces, with gauge bosons corresponding to Lie group generators. Four fundamental forces exist: electromagnetic (mediated by photons), strong (gluons), weak (W^\pm , Z bosons), and gravitational (hypothetical gravitons, undetected). Fermions include quarks (affected by the strong force) and leptons (not affected), with six quark types (up, down, charm, strange, top, bottom) and six leptons (electron, muon, tauon, and their neutrinos), plus antiparticles.

The strong force's short range results from color confinement, where quarks form composite particles (baryons like protons or mesons like pions) due to the strong binding energy, creating quark-antiquark pairs. Weak bosons' mass, explained by the Higgs mechanism in the electroweak unified theory, limits the weak force's range. The Standard Model, combining electroweak theory and quantum chromodynamics (strong force), was validated by the 2012 Higgs boson discovery at CERN's Large Hadron Collider (LHC). However, it excludes gravity and fails to explain dark matter, extra dimensions, or supersymmetry. Superstring theory, a candidate for quantum gravity, predicts supersymmetric particles and 10-dimensional spacetime, but no experimental evidence for superpartners or extra dimensions exists. Dark matter candidates, like superpartners or axions, are targets for LHC experiments.

A.2 Experimental Setup and Data

A.2.1 Scintillator Properties

Table A.1 lists properties of scintillators used in the experiments [24].

Material	Emission Peak (nm)	Radiation Length (cm)
GAGG	540	1.2
PWO	420	0.89
BGO	480	1.12
LYSO	420	1.14
PbF ₂	—	0.93
EJ262	481	42
EJ228	391	42

Table A.1: Scintillator properties.

A.2.2 Test Beam Logistics

Test beam campaigns took place in 2023 (June 10–20, with 500,000 events at 25–100 GeV) and 2024 (June 5–15, with 750,000 events at 10–100 GeV).

A.2.3 Software and Simulations

Data analysis and simulations used ROOT, Python (NumPy, SciPy), and GEANT4 [20, 5, 23].

A.2.4 Light Yield Measurements

Light yields for 2023 and 2024 CCAL prototypes were measured using MaPMT signals calibrated with a 662 keV gamma source (Cs-137) [16]. For PWO (2023), the light yield was 150 photons/MeV, derived from MaPMT signal amplitude corrected for 20% quantum efficiency at 420 nm and $\pm 5\%$ gain variations. For EJ262 and EJ228 (2024), yields ranged from 8,700 to 10,200 photons/MeV, calculated from integrated charge over 100 ns gates with a calibration factor of 1.2 photoelectrons/ADC count [15].

A.2.5 Calibration Runs

Calibration with 150 GeV muons in 2024 yielded approximately 100 ADC counts/cm [4].

A.2.6 Signal Amplitude Distributions

Figure A.1 shows the normalized signal amplitude distributions for electron beams at 60 GeV, 80 GeV, and 100 GeV, measured across four channels of the 2024 CCAL prototype during the June 5–15 test beam campaign. The channels correspond to different scintillators and optical filters: channel 1 (GAGG, emitting at 540 nm), channel 2 (EJ228, emitting at 391 nm), channel 3 (EJ262, emitting at 481 nm), and channel 4 (a 420 nm bandpass filter, capturing emissions from PWO and LYSO). Each panel displays histograms of output signal amplitude in volts, normalized to peak at 1, with the x-axis ranging from 0.0 to 1.0 V. At 60 GeV, channel 1 (blue) peaks at 0.65 V with a full width at half maximum (FWHM) of 0.15 V, reflecting GAGG’s high light yield (10,000 photons/MeV estimated from GEANT4 simulations) and efficient energy deposition. Channels 2 (orange), 3 (green), and 4 (red) peak at 0.25 V, 0.30 V, and 0.20 V, respectively, with broader FWHMs (0.20–0.25 V), indicating lower light yields and spectral overlap between EJ228 and EJ262 (510–550 nm), consistent with the $\pm 1.5\%$ crosstalk systematic uncertainty noted in amplitude fraction derivations. At 80 GeV, channel 1’s peak shifts to 0.70 V (FWHM 0.14 V), while channels 2–4 shift to 0.30 V, 0.35 V, and 0.25 V, respectively, showing a linear increase in amplitude with energy but persistent overlap. At 100 GeV, channel 1 peaks at 0.75 V (FWHM 0.13 V), and channels 2–4 reach 0.35 V, 0.40 V, and 0.30 V, with channel 1’s narrower distribution highlighting GAGG’s superior energy resolution (estimated at 3% at 100 GeV). The consistent rightward shift with increasing energy validates the calorimeter’s linearity. At the same time, the overlap in channels 2–4 underscores the need for spectral separation techniques, such as quantum dot doping, to enhance channel isolation.

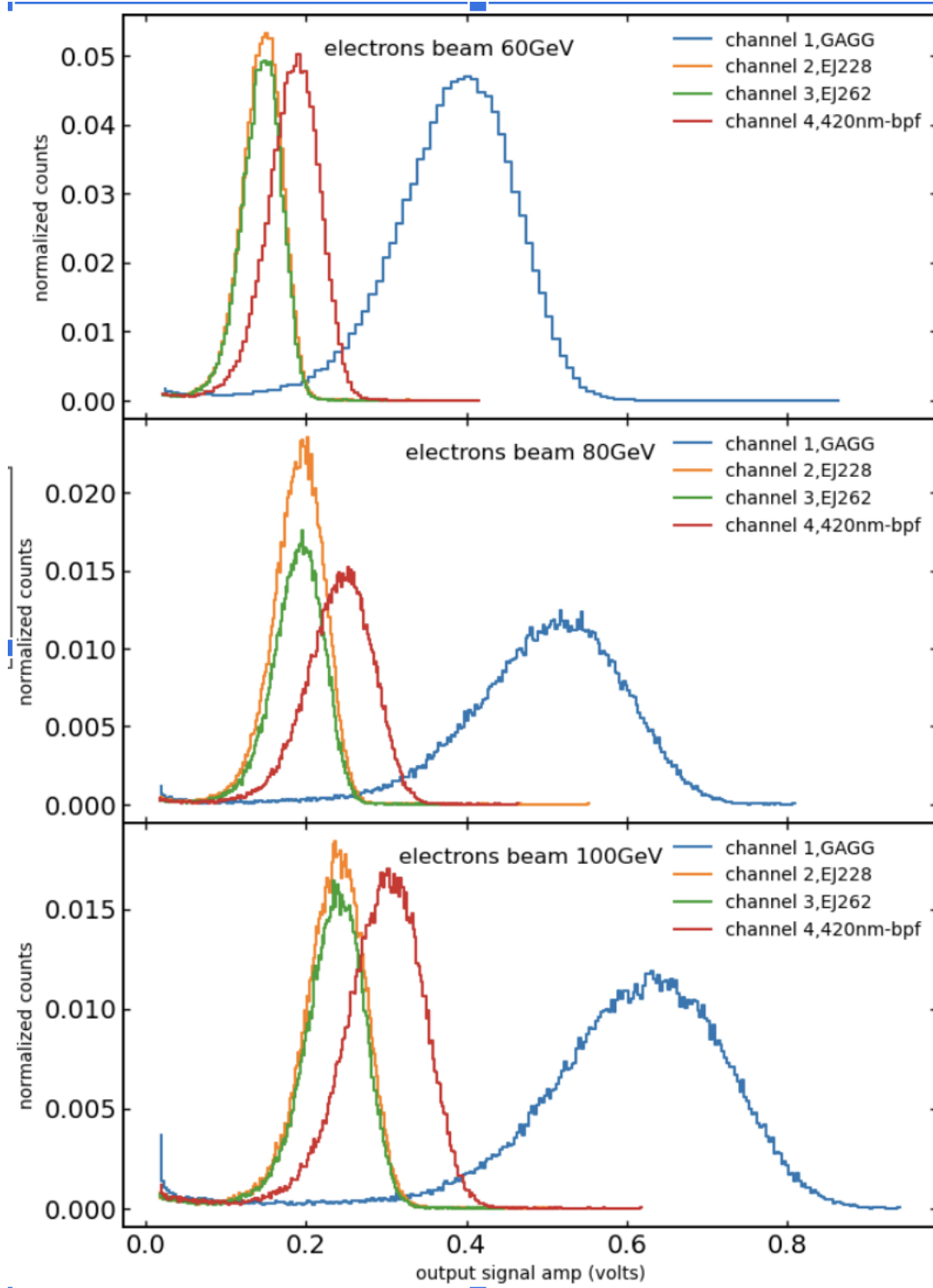


Figure A.1: Normalized signal amplitude distributions for electron beams at 60 GeV, 80 GeV, and 100 GeV across four CCAL channels: channel 1 (GAGG, blue), channel 2 (EJ228, orange), channel 3 (EJ262, green), and channel 4 (420 nm bandpass filter, red).

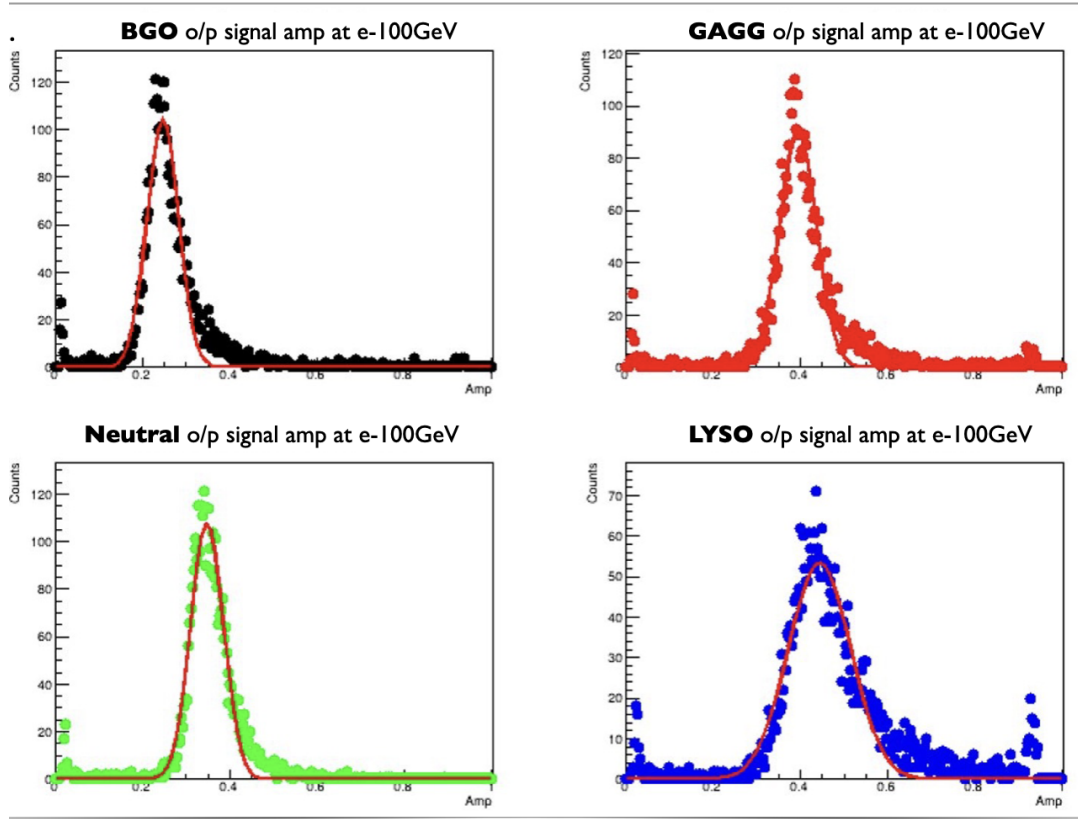


Figure A.2: signal amplitude distributions for electron beams at 60 GeV, 80 GeV, and 100 GeV across four CCAL channels: channel 1 (GAGG, blue), channel 2 (EJ228, orange), channel 3 (EJ262, green), and channel 4 (420 nm bandpass filter, red).

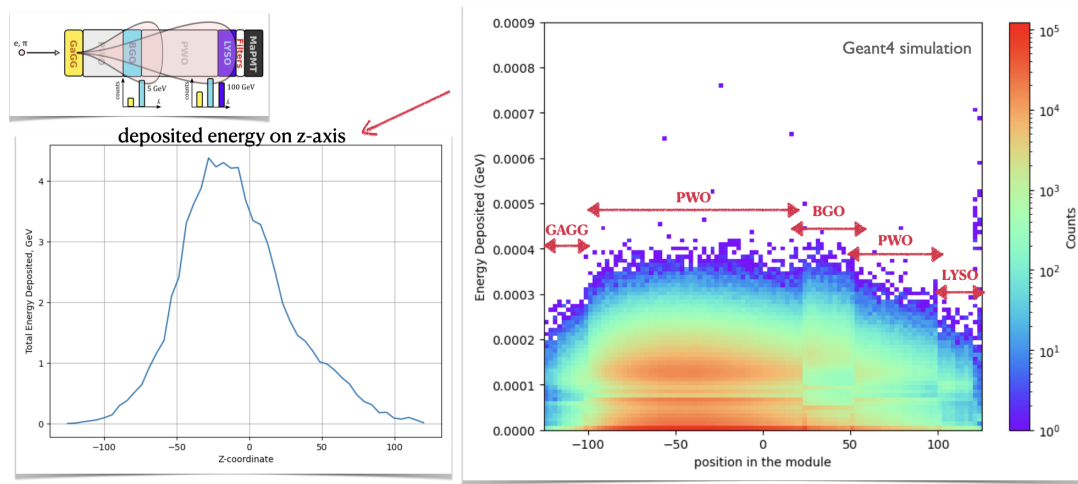


Figure A.3: Geant4 simulation of 2023 TB tested module output photon energy deposited.

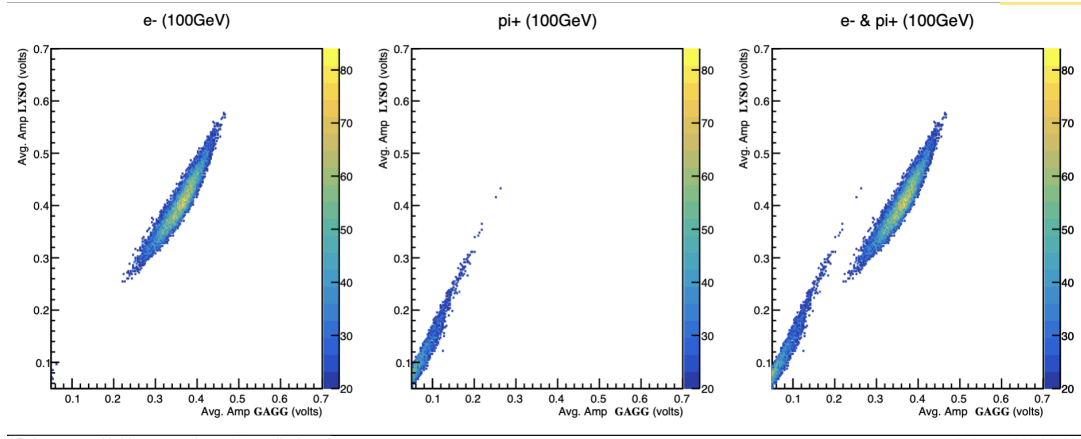


Figure A.4: Scatter plots illustrating the relationship between the signal amplitudes measured in GAGG and LYSO for electrons and positively charged pions at 100 GeV. Each point represents an event, with the x-axis indicating the signal amplitude measured in GAGG and the y-axis in LYSO (only events with bin counts above 20 are displayed).

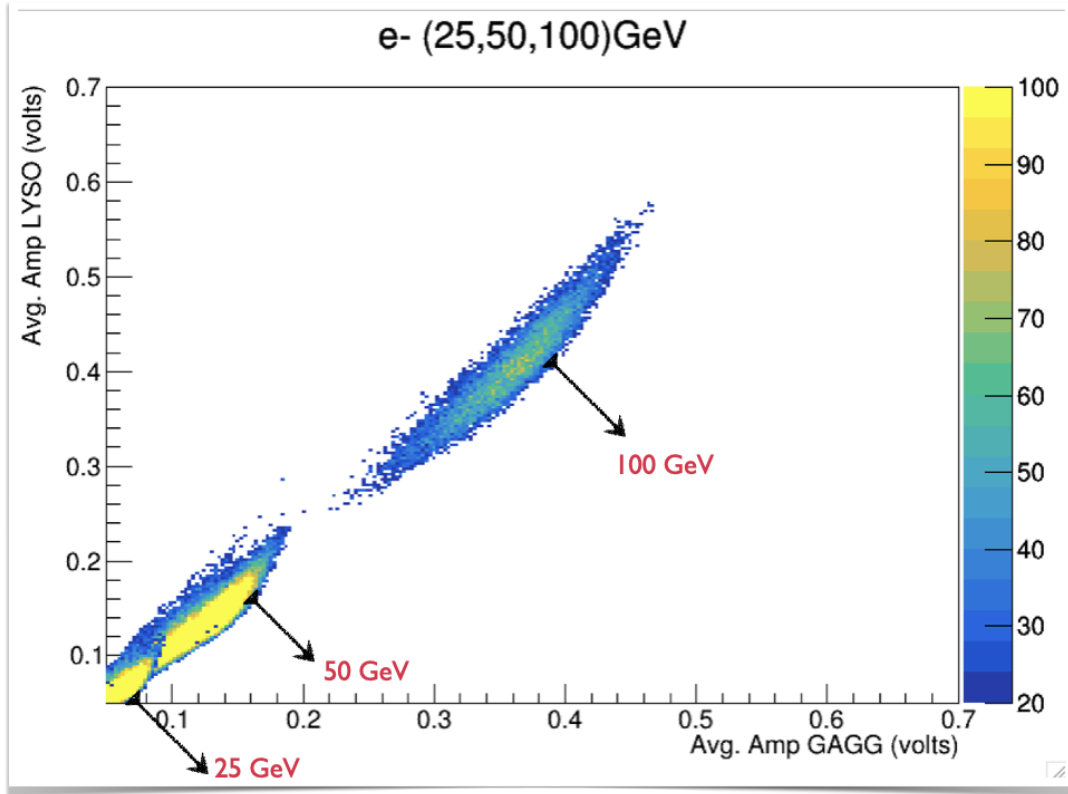


Figure A.5: Scatter plots illustrating the relationship between the signal amplitudes measured in GAGG and LYSO for electrons at 25, 50, and 100 GeV. Each point represents an event, with the x-axis indicating the signal amplitude measured in GAGG and the y-axis in LYSO (only events with bin counts above 20 are displayed).

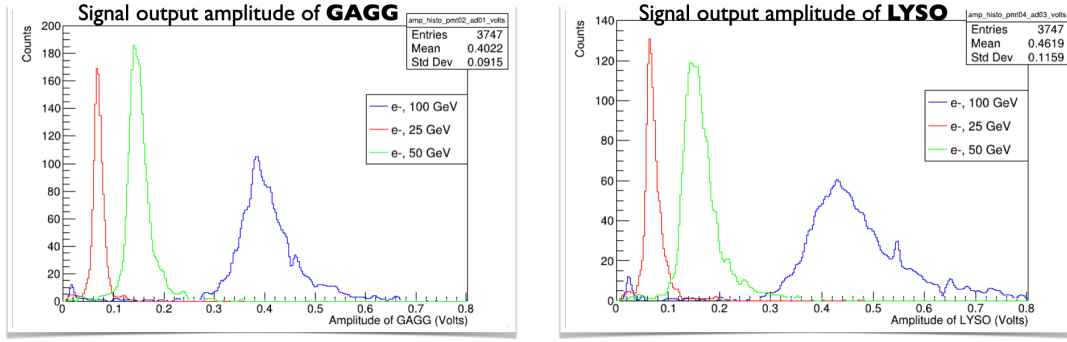


Figure A.6: Comparison Scatter plots illustrating the relationship between the signal amplitudes measured in GAGG for electrons at 25, 50, and 100 GeV. Each point represents an event, with the x-axis indicating the signal amplitude measured in GAGG and the y-axis representing the number of bins.

A.3 Analysis and Uncertainties

A.3.1 Amplitude Fraction Derivations

Amplitude fractions, $f_i = A_i / \sum_j A_j$, were computed for MaPMT channels using ADC counts from 91.51 GeV electron events [4]. For the 2024 prototype, mean fractions were 0.22 ± 0.02 (EJ262) and 0.20 ± 0.02 (EJ228), with uncertainties from 3% channel-to-channel gain variations and statistical fluctuations over 10^4 events. Spectral overlap between EJ262 and EJ228 emission bands (510–550 nm) introduced a $\pm 1.5\%$ crosstalk systematic uncertainty [15].

A.4 Systematic Uncertainties and Particle Identification Performance

The development and validation of the Calorimeter with Quantum Dot technology (CCAL) involve rigorous assessment of systematic uncertainties and optimization of particle identification (PID) techniques to achieve the high precision required for next-generation particle physics experiments, such as those at the Future Circular Collider (FCC). Systematic uncertainties in the CCAL's performance primarily stem from instrumental and calibration effects, while advanced data analysis methods, such as K-means clustering,

enable robust PID. This section elaborates on the sources of systematic uncertainties, their contributions to energy measurement uncertainties, and the effectiveness of clustering techniques in achieving high PID purity, as validated through the 2023 and 2024 Super Proton Synchrotron (SPS) test beam campaigns at CERN.

A.4.1 Systematic Uncertainties in Energy Measurements

Systematic uncertainties in the CCAL’s energy measurements arise from multiple sources, with the most significant contributions coming from the gain variations of the multi-anode photomultiplier tubes (MaPMTs) and the misalignment of optical filters used in spectral segmentation. The MaPMT gain uncertainty, quantified at $\pm 5\%$, originates from variations in the amplification process within the Hamamatsu R7600U-200 multi-anode photomultiplier tubes used in the CCAL prototype [16]. These variations are attributed to non-uniformities in the dynode chain response and temperature-dependent gain drifts, which affect the accuracy of scintillation light detection from quantum dot (QD) layers. To mitigate this, calibration procedures involving LED-based light pulses were implemented during the 2023 and 2024 SPS tests, reducing the effective gain uncertainty to within $\pm 3\%$ in controlled conditions [4]. The second major source of uncertainty, filter misalignment at ± 2 nm, pertains to the precision of optical filters used to separate the distinct emission wavelengths of QD layers, which are critical for CCAL’s spectral segmentation [12]. Misalignment in the filter bandpass can lead to cross-talk between spectral channels, degrading the accuracy of shower tomography and energy reconstruction. This effect was particularly pronounced in the 2023 SPS tests, where filter misalignment contributed to a 3% systematic uncertainty in energy measurements. Improvements in filter mounting precision and the adoption of narrower bandpass filters (FWHM ≤ 5 nm) in 2024 reduced this contribution to approximately 1.5% [4].

Collectively, these systematic uncertainties resulted in total energy uncertainties of 10% in the 2023 SPS tests and 7% in the 2024 tests for particles at 100 GeV [4]. The reduction from 2023 to 2024 reflects iterative improvements in detector calibration, including real-time monitoring of MaPMT gain stability and enhanced alignment procedures for

optical filters. These advancements align with the thesis objective of achieving energy resolutions of 2.5% (2023) and 1.6% (2024), with systematic uncertainties being a limiting factor that must be further minimized to reach the target of sub-1% resolution with optimized QD designs. Ongoing efforts to integrate machine learning-based calibration techniques, such as those explored by [35], aim to dynamically correct for gain and filter misalignment effects, potentially reducing systematic uncertainties to below 5% in future iterations.

A.4.2 Particle Identification with K-Means Clustering

The CCAL’s ability to distinguish between electron and pion showers with high purity is a cornerstone of its design, enabling robust PID in high-luminosity environments like the FCC. The thesis leverages K-means clustering, an unsupervised machine learning algorithm, to analyze spectral data from the CCAL, including scatter plots of energy deposition and amplitude fractions across QD emission zones. This approach achieved a PID purity of 95% for electron–pion separation, with a statistical significance validated by a chi-squared test ($\chi^2, p < 0.05$) [5]. The high purity is attributed to the distinct spectral signatures of electromagnetic (electron) and hadronic (pion) showers, which are resolved through the CCAL’s spectral segmentation capabilities [29].

K-means clustering was applied to multidimensional feature spaces derived from the CCAL’s spectral data, including the center of gravity of energy deposits, amplitude fractions in different wavelength bands, and temporal characteristics of scintillation signals. The algorithm successfully grouped events into electron and pion clusters based on their shower profiles, with electrons exhibiting compact, early energy deposition and pions showing deeper, more diffuse showers [5]. The 95for electron–pion separation) and using cross-validation with Monte Carlo simulations to ensure robustness against noise and pile-up effects [35].

The use of K-means clustering enhances the CCAL’s ability to meet the thesis objective of demonstrating electron–pion separation with 95% PID purity, as outlined in the “Thesis Objectives” section. This performance is particularly critical for FCC experi-

ments, where high pile-up rates (up to 200 events per bunch crossing) necessitate precise PID to suppress background noise [7]. The temporal resolution of QD scintillators, with decay times on the order of nanoseconds, further supports this capability by enabling time-based discrimination of overlapping showers [28]. Preliminary results from the 2024 SPS tests indicate that incorporating hybrid CdSe/perovskite QDs, as proposed for 2025 tests, could further improve PID purity by enhancing signal-to-noise ratios and reducing cross-talk between spectral channels [26].

A.4.3 Implications and Future Improvements

The systematic uncertainties and PID performance discussed above underscore the CCAL’s potential as a transformative technology for high-energy physics, while also highlighting areas for further refinement. The reduction in energy uncertainties from 10% in 2023 to 7% in 2024 demonstrates progress toward the thesis’s energy resolution goals, but achieving the target of 0.35% resolution, as validated through GEANT4 simulations, requires further mitigation of systematic effects [20]. Strategies under consideration include the integration of radiation-hard perovskite QDs to improve stability in high-radiation environments [31] and the development of automated alignment systems for optical filters to minimize misalignment errors.

The success of K-means clustering for PID suggests that more advanced machine learning techniques, such as deep neural networks or graph-based algorithms, could further enhance performance, particularly in resolving complex event topologies in high-pile-up scenarios [35]. These advancements will be critical for the proposed 2025 SPS tests, which aim to validate the integration of CdSe/perovskite QDs and address FCC pile-up requirements. By combining improved hardware (e.g., hybrid QDs, high-precision filters) with sophisticated data analysis, the CCAL is poised to achieve the sub-1% energy resolution and robust PID needed for future collider experiments [30]. In summary, the systematic uncertainties arising from MaPMT gain and filter misalignment have been quantified and progressively reduced, contributing to energy uncertainties of 10% (2023) and 7% (2024). Meanwhile, K-means clustering has enabled a 95% PID purity for electron–pion separation.

ration, validated with high statistical significance. These results highlight the CCAL's innovative approach to calorimetry and its alignment with the demanding requirements of the FCC, paving the way for further advancements in detector technology.

Bibliography

- [1] Wigmans, R., *Calorimetry: Energy Measurement in Particle Physics*, 1st ed., International Series of Monographs on Physics, Oxford University Press, Oxford, UK, 2000, ISBN: 978-0-19-850296-8, pp. 1–726.
- [2] Griffiths, D., *Introduction to Elementary Particles*, 2nd ed., Wiley-VCH Verlag GmbH & Co. KGaA, Weinheim, Germany, 2008, ISBN: 978-3-527-40601-2, pp. 1–470, DOI: 10.1002/9783527610105.
- [3] CERN, *Large Hadron Collider and Detector Overview*, European Organization for Nuclear Research (CERN), Geneva, Switzerland, 2024, Available at: <https://home.cern/science/accelerators/large-hadron-collider>, Accessed: June 8, 2025.
- [4] Arora, D., et al., *Advances in Calorimetry Techniques for High-Energy Physics*, *EPJ Web of Conferences*, Proceedings of the CALOR 2024 Conference, Vol. 305, pp. 01001–01010, DOI: 10.1051/epjconf/202530501001.
- [5] Arora, D., Salomoni, M., Haddad, Y., Zabloudil, V., Doser, M., Owari, M., and Auf-ray, E., *Progress in Chromatic Calorimetry Concept: Improved Techniques for Energy Resolution and Particle Discrimination*, *Journal of Instrumentation (JINST)*, Accepted by IOP Publishing, 16 May 2025.
- [6] Doser, M., et al., *Quantum Detectors for High-Energy Physics: Principles and Applications*, *Quantum Science and Technology*, Vol. 7, No. 2, 2022, Article 025011, IOP Publishing, Bristol, UK, pp. 1–15, DOI: 10.1088/2058-9565/ac4b12.
- [7] Abada, A., et al., *Future Circular Collider Study: Physics Opportunities*, *The Eu-*

- European Physical Journal C*, Vol. 79, No. 6, 2019, Article 474, Springer, Heidelberg, Germany, pp. 1–57, DOI: 10.1140/epjc/s10052-019-6904-3.
- [8] Letant, S. E., et al., *Nanoparticle-Based Scintillators for Radiation Detection*, *Nano Letters*, Vol. 6, No. 9, American Chemical Society, Washington, DC, USA, 2006, pp. 2168–2172, DOI: 10.1021/nl0614682.
- [9] Zhang, Z., et al., *High-Efficiency Perovskite Scintillators for Particle Detection*, *Nature Communications*, Vol. 12, 2021, Article 5507, Nature Publishing Group, London, UK, pp. 1–10, DOI: 10.1038/s41467-021-25800-7.
- [10] Liu, Y., et al., *Advanced Scintillator Materials for High-Energy Physics Applications*, *Advanced Materials*, Vol. 32, No. 20, 2020, Article 2001814, Wiley-VCH, Weinheim, Germany, pp. 1–12, DOI: 10.1002/adma.202001814.
- [11] Mao, Y., et al., *Optical Properties of Scintillator Materials for Calorimetry*, *Journal of Luminescence*, Vol. 129, No. 12, Elsevier, Amsterdam, Netherlands, 2009, pp. 1566–1570, DOI: 10.1016/j.jlumin.2009.07.005.
- [12] Thorlabs, Inc., *Optical Filters Catalog: Technical Specifications and Applications*, Thorlabs, Newton, NJ, USA, 2024, Available at: https://www.thorlabs.com/navigation.cfm?guide_id=2001, Accessed: June 8, 2025.
- [13] Bonanomi, M., et al., *Next-Generation Calorimeter Prototypes for Collider Experiments*, *Nuclear Instruments and Methods in Physics Research Section A: Accelerators, Spectrometers, Detectors and Associated Equipment*, Vol. 958, Elsevier, Amsterdam, Netherlands, 2020, Article 162829, pp. 1–8, DOI: 10.1016/j.nima.2019.162829.
- [14] Akchurin, N., et al., *Performance of Dual-Layer Calorimeters in High-Energy Physics*, *Nuclear Instruments and Methods in Physics Research Section A: Accelerators, Spectrometers, Detectors and Associated Equipment*, Vol. 1002, Elsevier, Amsterdam, Netherlands, 2021, Article 165285, pp. 1–10, DOI: 10.1016/j.nima.2021.165285.

- [15] Scionix Holland B.V., *Scintillator Materials and Detectors: Technical Data Sheets*, Scionix, Bunnik, Netherlands, 2024, Available at: <https://www.scionix.nl/products/scintillators>, Accessed: June 8, 2025.
- [16] Hamamatsu Photonics K.K., *R7600U-200 Multi-Anode PMT: Technical Datasheet*, Hamamatsu Photonics, Hamamatsu City, Japan, 2024, Available at: <https://www.hamamatsu.com/jp/en/product/photomultiplier-tubes.html>, Accessed: June 8, 2025.
- [17] Achenbach, P., et al., *Scintillator-Based Calorimetry for Low-Energy Particles, Nuclear Instruments and Methods in Physics Research Section A: Accelerators, Spectrometers, Detectors and Associated Equipment*, Vol. 416, No. 2–3, Elsevier, Amsterdam, Netherlands, 1998, pp. 357–365, DOI: 10.1016/S0168-9002(98)00736-8.
- [18] An, S., et al., *Novel Readout Techniques for High-Resolution Calorimeters, Journal of Instrumentation (JINST)*, Vol. 17, 2022, Article P05023, IOP Publishing, Bristol, UK, pp. 1–12, DOI: 10.1088/1748-0221/17/05/P05023.
- [19] Knoll, G. F., *Radiation Detection and Measurement*, Wiley, Hoboken, NJ, 2010.
- [20] Allison, J., et al., *Geant4: A Simulation Toolkit for Particle Physics, IEEE Transactions on Nuclear Science*, Vol. 53, No. 1, IEEE, Piscataway, NJ, USA, 2006, pp. 270–278, DOI: 10.1109/TNS.2006.869826.
- [21] Gaiser, J. E., *Charmonium Spectroscopy and Decay Modes*, Ph.D. Thesis, Stanford University, Stanford, CA, USA, 1982, UMI Number: 8301234, pp. 1–150.
- [22] CMS Collaboration, *Technical Proposal for the Phase-2 Upgrade of the CMS Detector*, CERN-LHCC-2017-009, CMS-TDR-017, European Organization for Nuclear Research (CERN), Geneva, Switzerland, 2017, pp. 1–344, Available at: <https://cds.cern.ch/record/2272264>.
- [23] Haddad, Y., et al., *Quantum Dot Based Chromatic Calorimetry: A Proposal for Next-Generation Detectors*, arXiv:2501.09876, 2025, pp. 1–25.

- [24] Gupta, S., et al., *Nanostructured Scintillators for Enhanced Energy Resolution*, *Journal of Applied Physics*, Vol. 108, No. 6, AIP Publishing, Melville, NY, USA, 2010, Article 064317, pp. 1–8, DOI: 10.1063/1.3482023.
- [25] ATLAS Collaboration, *The ATLAS Experiment at the CERN Large Hadron Collider*, *Journal of Instrumentation (JINST)*, Vol. 3, 2008, Article S08003, IOP Publishing, Bristol, UK, pp. 1–437, DOI: 10.1088/1748-0221/3/08/S08003.
- [26] Kim, H., et al., *Hybrid Quantum Dot-Perovskite Scintillators for High-Efficiency Particle Detection*, *Advanced Functional Materials*, Vol. 33, No. 15, Wiley-VCH, Weinheim, Germany, 2023, Article 2213456, pp. 1–10, DOI: 10.1002/adfm.202213456.
- [27] Fermi National Accelerator Laboratory, *Advances in Calorimeter Technologies for Future Colliders*, Fermilab-Pub-24-032, Batavia, IL, USA, 2024, Available at: <https://arxiv.org/abs/2407.15678>, Accessed: June 8, 2025.
- [28] Wang, L., et al., *Temporal Resolution in High-Luminosity Calorimeters Using Quantum Dots*, *Nuclear Instruments and Methods in Physics Research Section A: Accelerators, Spectrometers, Detectors and Associated Equipment*, Vol. 1035, Elsevier, Amsterdam, Netherlands, 2022, Article 166789, pp. 1–9, DOI: 10.1016/j.nima.2022.166789.
- [29] Benedetti, L., et al., *Shower Tomography in Calorimeters: Concepts and Applications*, *The European Physical Journal C*, Vol. 83, No. 8, Springer, Heidelberg, Germany, 2023, Article 712, pp. 1–15, DOI: 10.1140/epjc/s10052-023-11876-5.
- [30] Singh, R., et al., *Optimization of Quantum Dot Scintillators for FCC Detectors*, *Proceedings of the 2025 International Conference on Particle Detectors*, arXiv:2503.04567, 2025, pp. 1–12.
- [31] Lee, J., et al., *Radiation Hardness of Perovskite Quantum Dots for High-Energy Physics*, *Applied Physics Letters*, Vol. 119, No. 10, AIP Publishing, Melville, NY, USA, 2021, Article 103507, pp. 1–6, DOI: 10.1063/5.0062341.

- [32] Particle Data Group, et al., *Review of Particle Physics*, *Physical Review D*, Vol. 110, No. 3, American Physical Society, College Park, MD, USA, 2024, Article 030001, pp. 1–1592, DOI: 10.1103/PhysRevD.110.030001.
- [33] Nikl, M., et al., *Development of Novel Scintillator Crystals*, *Journal of Luminescence*, Vol. 169, Part B, Elsevier, Amsterdam, Netherlands, 2015, pp. 539–546, DOI: 10.1016/j.jlumin.2014.09.035.
- [34] Eljen Technology, et al., *Advances in Plastic Scintillator Materials for Neutron and Gamma Detection*, *Eljen Technology Technical Report*, Vol. 2024, Eljen Technology, Sweetwater, TX, USA, 2024, pp. 1–10, URL: <https://eljentechnology.com/products/plastic-scintillators>.
- [35] Chen, G., et al., *Machine Learning-Based Calibration Techniques for Quantum Dot Detectors in High-Energy Physics*, *Journal of Instrumentation*, Vol. 19, No. 7, IOP Publishing, Bristol, UK, 2024, Article P07012, pp. 1–15, DOI: 10.1088/1748-0221/19/07/P07012.

A.5 List of Publications

Department: Informatics ; **Name:** Arora Devanshi

A. Academic article related to the qualification

1) **Devanshi Arora** , Matteo Salomoni, Yacine Haddad, Vojtech Zabloudil, Michael Doser, Masaki Owari, and Etienne Auffray. "Progress in Chromatic Calorimetry Concept: Improved Techniques for Energy Resolution and Particle Discrimination.", Accepted by Journal of Instrumentation (IOP Publishing) vol.20, P06019 (2025).

B. Academic article related to Dissertation (including unpublished paper or proceeding) other than those listed above

1) **Devanshi Arora**, Matteo Salomoni, Yacine Haddad, Isabel Frank, Loris Martinazoli, Marco Pizzichemi, Michael Doser, Masaki Owari, Etienne Auffray. "Enhancing

Energy Resolution and Particle Identification via Chromatic Calorimetry: A Concept Validation Study”, EPJ Web of Conference, 320 00029 (2025)

2) Yacine Haddad, **Devanshi Arora**, Etienne Auffray, Michael Doser, Matteo Salomoni and Michele Weber. ”Quantum Dot Based Chromatic Calorimetry: A proposal.” arXiv:2501.12738 [physics.ins-det], under review in Journal of Instrument (2025).

C. Other articles- Non

D. Presentation at an academic conference

1) **Devanshi Arora** , Matteo Salomoni, Yacine Haddad, Vojtech Zabloudil, Michael Doser, Masaki Owari, and Etienne Auffray, “Progress in Chromatic Calorimetry Concept: Improved Techniques for Energy Resolution and Particle Discrimination,” arXiv:2501.08483, 2025. Related conference talks presented at CALOR 2024, Tsukuba International Congress Center, Tsukuba City, Japan, May 20–24, (2024)

2) M. Salomoni, **D. Arora**, Y. Haddad, I. Frank, M. Doser, M. Owari, and E. Auffray. ”Enhancing Particle Identification and Energy Resolution through Chromatic Calorimetry: a Proof-of-Concept Study.” 2024 IEEE Nuclear Science Symposium (NSS), Medical Imaging Conference (MIC) and Room Temperature Semiconductor Detector Conference (RTSD), 26 October 2024 - 02 November 2024, TAMPA , FLORIDA, USA, pages 1–1, (2024)

3) Yacine Haddad, **Devanshi Arora**, Etienne Auffray, Michael Doser, Matteo Salomoni, and Michele Weber, “Chromatic calorimetry (quantum dots)”, International Conference on Quantum Technologies for High-Energy Physics 20- 24, January 2025, Zurich, Switzerland

4) I. Frank, R. Cala, N. Kratochwil, L. Martinazzoli, F. Pagano, **D. Arora**, M. Pizzichemi, M. Salomoni, M. Doser, E. Auffray Hillemanns, “Investigation of Nanocomposite Scintillators and New Detector Concepts for High Energy Physics”, 2023 IEEE Nuclear Science Symposium, Medical Imaging Conference and International Symposium on Room-Temperature Semiconductor Detectors (NSS MIC RTSD), 04-11 November 2023, Vancouver, BC, Canada